JEM Journal of Experimental Medicine

ARTICLE

Activating NO–sGC crosstalk in the mouse vascular niche promotes vascular integrity and mitigates acute lung injury

Hao He[1,2*], Wu Yang[1,2*], Nan Su[1,2*], Chuankai Zhang[3], Jianing Dai[1], Feng Han[1], Mahak Singhal[4], Wenjuan Bai[5], Xiaolan Zhu[1,2], Jing Zhu[1,2], Zhen Liu[2,6], Wencheng Xia[1,2], Xiaoting Liu[1,2], Chonghe Zhang[1,2], Kai Jiang[1], Wenhui Huang[7], Dan Chen[1], Zhaoyin Wang[1,2], Xueyang He[1,2], Frank Kirchhoff[7], Zhenyu Li[8], Cong Liu[1,2], Jingning Huan[3], Xiaohong Wang[9], Wu Wei[2,6], Jing Wang[5], Hellmut G. Augustin[10,11], and Junhao Hu[1,2]

Disruption of endothelial cell (ECs) and pericytes interactions results in vascular leakage in acute lung injury (ALI). However, molecular signals mediating EC–pericyte crosstalk have not been systemically investigated, and whether targeting such crosstalk could be adopted to combat ALI remains elusive. Using comparative genome-wide EC–pericyte crosstalk analysis of healthy and LPS-challenged lungs, we discovered that crosstalk between endothelial nitric oxide and pericyte soluble guanylate cyclase (NO–sGC) is impaired in ALI. Indeed, stimulating the NO–sGC pathway promotes vascular integrity and reduces lung edema and inflammation-induced lung injury, while pericyte-specific sGC knockout abolishes this protective effect. Mechanistically, sGC activation suppresses cytoskeleton rearrangement in pericytes through inhibiting VASP-dependent F-actin formation and MRTFA/SRF-dependent de novo synthesis of genes associated with cytoskeleton rearrangement, thereby leading to the stabilization of EC–pericyte interactions. Collectively, our data demonstrate that impaired NO–sGC crosstalk in the vascular niche results in elevated vascular permeability, and pharmacological activation of this crosstalk represents a promising translational therapy for ALI.

Introduction

Vascular integrity is essential for maintaining tissue homeostasis (Park-Windhol and D'Amore, 2016). The disruption of vascular integrity, followed by increased pulmonary edema and impaired gas exchange in the lungs, is key pathological changes of acute lung injury (ALI) and its more severe form, the acute respiratory distress syndrome (ARDS). ALI and ARDS are life-threatening conditions caused by systemic sepsis, traumatic injury, or severe bacterial or viral pneumonia, including COVID-19 (Copin et al., 2020; Teuwen et al., 2020; Xu et al., 2020). Mortality among severe ARDS patients remains high at 20–25% in recent placebo-controlled trials (Matthay et al., 2019). Currently, no specific pharmacotherapies have been developed and supportive mechanical ventilation remains the mainstay of treatment (Matthay et al., 2019; Thompson et al., 2017). In past decades, many modalities to treat ALI have been tested, including administering glucocorticoids or neutralizing antibodies against IL-6 and other inflammatory cytokines (Cala-Garcia et al., 2020; Villar et al., 2020). Nevertheless, the clinical benefits of these strategies for reducing ALI's severity and mortality remain controversial. While disruption of the alveolar vascular barrier is the fundamental pathological change with ALI (Matthay et al., 2019; Teuwen et al., 2020), strategies to reinstate vascular integrity, e.g., activating endothelial Tie2 using a novel angiopoietin2-binding and TIE2-activating antibody, to ameliorate lung injury and improve survival have only recently gained attention (Han et al., 2016).

[1]Interdisciplinary Research Center on Biology and Chemistry, Shanghai Institute of Organic Chemistry, Chinese Academy of Sciences, Shanghai, China; [2]University of Chinese Academy of Sciences, Beijing, China; [3]Department of Burn and Plastic Surgery, Ruijin Hospital, Shanghai Jiao Tong University School of Medicine, Shanghai, China; [4]Laboratory of AngioRhythms, European Center for Angioscience, Medical Faculty Mannheim, Heidelberg University, Mannheim, Germany; [5]Shanghai Institute of Immunology, Shanghai Jiao Tong University School of Medicine, Shanghai, China; [6]Chinese Academy of Sciences Key Laboratory of Computational Biology, Shanghai Institute of Nutrition and Health, Chinese Academy of Sciences, Shanghai, China; [7]Department of Molecular Physiology, Center for Integrative Physiology and Molecular Medicine, University of Saarland, Homburg, Germany; [8]Texas A&M Health Science Center, Bryan, TX; [9]Department of Pharmacology and Tianjin Key Laboratory of Inflammation Biology, School of Basic Medical Sciences, Tianjin Medical University, Tianjin, China; [10]Division of Vascular Oncology and Metastasis, German Cancer Research Center (DKFZ-ZMBH Alliance), Heidelberg, Germany; [11]Department of Vascular Biology and Tumor Angiogenesis, European Center for Angioscience, Medical Faculty Mannheim, Heidelberg University, Mannheim, Germany.

*H. He, W. Yang, and N. Su contributed equally to this paper. Correspondence to Junhao Hu: jhhu@sioc.ac.cn.

The barrier function of blood vessels is controlled not only by endothelial cells (ECs), but also by pericytes that reside outside the endothelium. Reduced pericyte coverage or impaired EC–pericyte crosstalk leads to increased vascular leakage in various pathological conditions (Armulik et al., 2010; Daneman et al., 2010; Morikawa et al., 2002). Several molecular signals mediating EC–pericyte communications to control vessel development, maturation, and homeostasis have been discovered. During angiogenesis, EC-secreted platelet-derived growth factor (PDGFB) recruits pericytes by activating its cognate receptor PDGFRβ on pericytes. The disruption of PDGFB–PDGFRβ crosstalk by either *Pdgfb* or *Pdgfrb* knockout or through PDGFB-neutralizing antibody results in pericyte deficiency and vascular leakage (Armulik et al., 2010; Daneman et al., 2010; Leveen et al., 1994; Uemura et al., 2002). Similarly, endothelial JAG1 has been found to activate NOTCH3 on recruited pericytes and promote pericyte differentiation (Joutel et al., 1996; Machuca-Parra et al., 2017; Wang et al., 2014). Furthermore, pericyte-secreted angiopoietin-1 (ANGPT1) was found to activate the endothelial TIE2 receptor, thereby promoting vascular integrity and maturation (Augustin et al., 2009; Suri et al., 1996; Thurston et al., 1999). Despite the pivotal importance of EC–pericyte interaction in maintaining vascular homeostasis, most published studies have employed a candidate-based loss-of-function or gain-of-function approach; a systemic genome-wide characterization of molecular communications that underlie EC–pericyte interaction remains elusive.

Employing an intratracheal LPS-instilled ALI model, we establish the bidirectional communication landscape between ECs and pericytes by performing a genome-wide intercellular crosstalk analysis in lungs of healthy and ALI mice. We found the nitric oxide and soluble guanylate cyclase (NO–sGC) signaling was disrupted in the lungs of LPS-treated mice, as manifested in pericyte detachment, the loss of endothelial integrity, and the infiltration of inflammatory cells. Bolstering NO–sGC signaling through the post-injury administration of the sGC stimulator Riociguat prevented pericyte detachment and reinstated vascular barrier function. Mechanistically, sGC activation suppresses inflammation-induced cytoskeleton rearrangements in pericytes, therefore inhibiting the retraction of cytoplasmic processes over alveolar capillaries. Collectively, by establishing the first-ever EC–pericyte crosstalk landscape, our data identify NO–sGC as a therapeutically relevant signaling pathway for promoting vascular integrity and ameliorating ALI.

Results

Comparative EC–pericyte crosstalk analysis of healthy and LPS-instilled lungs

To establish a comprehensive EC–pericyte crosstalk landscape of healthy lung vasculature, we isolated ECs ($CD31^+/CD45^-/Ter119^-/Podoplanin^-/GFP^-$) and pericytes ($GFP^+/CD31^-/CD45^-/Ter119^-/Podoplanin^-$) from the lungs of Pdgfrb-EGFP mice and performed whole-genome transcriptomic profiling (Fig. 1 A and Fig. S1, A–C). In line with a recent publication (Figueiredo et al., 2020), the majority of EGFP + cells in the lungs of *Pdgfrb-EGFP::SM22a-CreER^{T2}::Rosa26-LSL-tdTomato* mice were pericytes ($EGFP^+/tdTomato^-$). Only a small fraction (~7%) were vascular smooth muscle cells (vSMCs; $EGFP^+/tdTomato^+$; Fig. S1 D), suggesting that the bulk RNA sequencing (RNA-seq) primarily reflected the transcriptome of lung pericytes. All genes with expression levels of transcripts per million (TPM) ≥ 2 were subjected to an expanded cell–cell interaction database (see details on the construction of the cell–cell interaction database in the Materials and methods section), which contains 2388 secreted ligand–receptor interactions, 354 membrane-anchored ligand–receptor interactions, and 82 interactions between small signaling molecule-generating enzymes and their cognate receptors (Fig. 1 A). After database filtering, 677 putative EC→pericyte interactions, and 681 putative pericyte→EC interactions in healthy lung vasculature were retrieved (Fig. 1 B). Biological pathway enrichment indicates that most of the EC–pericyte interactions were involved in the processes of blood vessel development, cell migration, cell adhesion, and inflammatory response (Fig. 1 C).

Next, to construct the EC–pericyte crosstalk landscape of diseased lung vasculature, we intratracheally instilled LPS into the *Pdgfrb-EGFP* mice to induce ALI, as characterized by impaired vascular integrity, increased lung edema, and immune cell infiltration (Matthay et al., 2019). 24 h later, we isolated ECs and pericytes and performed transcriptomic profiling (Fig. S1 E). Subsequently, the transcriptomes of EC and pericyte from healthy and ALI mice were analyzed. Interestingly, we found the number of differentially expressed genes (DEGs) was significantly higher in pericytes than in ECs (1,565 upregulated and 1,011 downregulated in pericytes vs. 197 upregulated and 218 downregulated in ECs; Fig. 1 D and Fig. S1 F). DEGs in pericytes were highly enriched for leukocyte migration and cytokine production (Fig. 1 E), supporting the emerging notion that pericytes play an essential role in controlling local inflammatory responses (Duan et al., 2018; Hurtado-Alvarado et al., 2014; Rustenhoven et al., 2017; Torok et al., 2021). Next, we submitted all genes expressed in ECs and pericytes to the cell–cell interaction database to construct the EC–pericyte crosstalk landscape of ALI mice, which was further compared with the healthy EC–pericyte crosstalk landscape to identify dysregulated EC–pericyte interactions. We found that 245 EC→pericyte interactions (101 upregulated, 144 downregulated) and 294 pericyte→EC interactions (148 upregulated, 146 downregulated) were significantly altered in LPS-instilled mice (Fig. 1 F). Biological pathway analysis revealed altered EC–pericyte interactions involved in the regulation of chemotaxis, cell migration, cell adhesion, angiogenesis, and vascular development (Fig. 1 G).

Impairment of the NO–sGC crosstalk during ALI

Focusing on the dysregulated interactions, we found that *Angpt1-Tek*—a well-described vascular-specific pathway that maintains vascular integrity (Augustin et al., 2009)—was among the top 10 most significantly downregulated pericyte→EC interactions (Fig. 2 A). Intriguingly, *Nos3-Gucy1a1* and *Nos3-Gucy1b1* were ranked as the top two most significantly downregulated EC→pericyte interactions (Fig. 2 A). *Nos3* encodes the NO-producing enzyme endothelial nitric oxide synthase (eNOS), whereas *Gucy1a1* and *Gucy1b1* encode the α1 and β1 subunits of

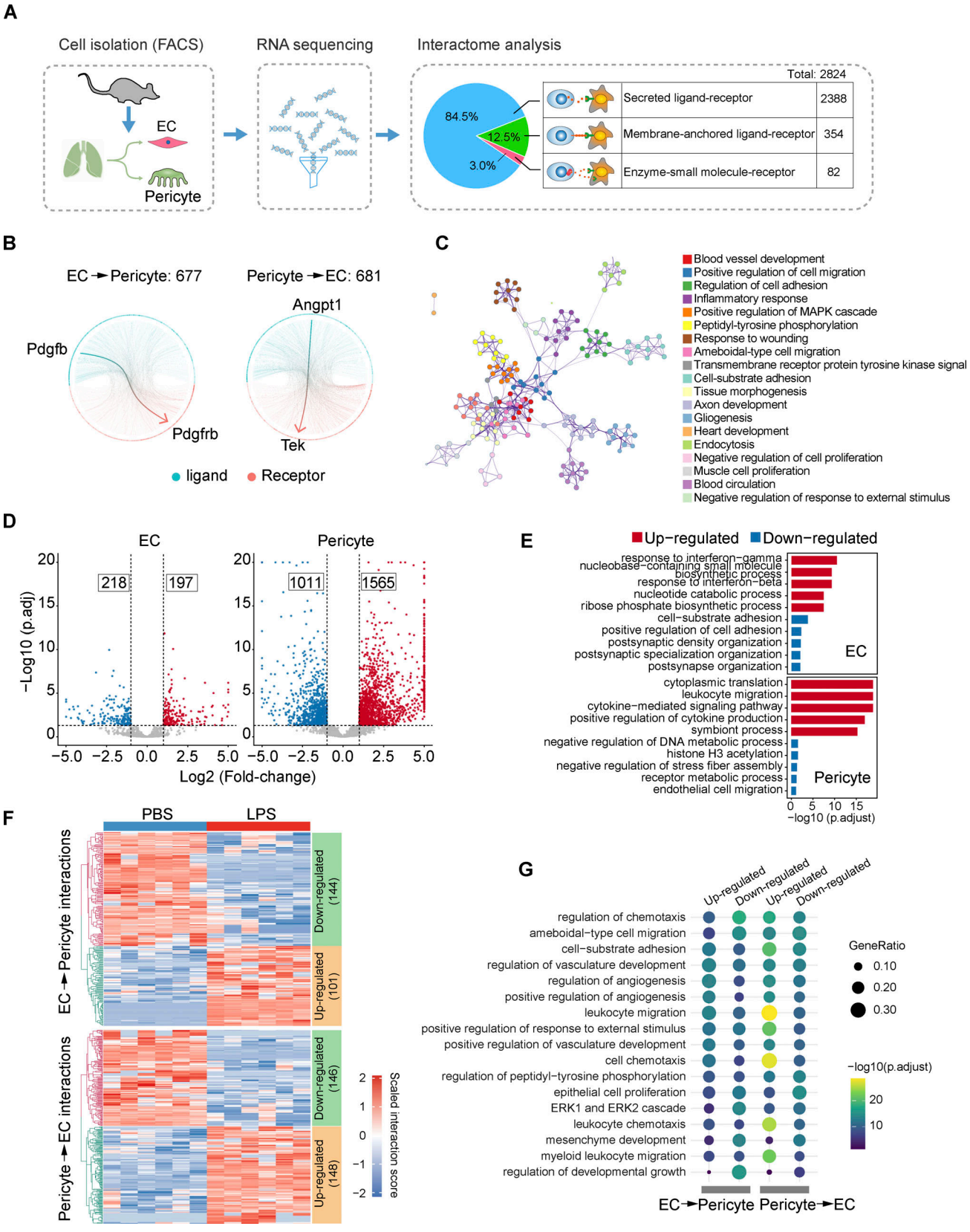

Figure 1. **Comparative EC–pericyte crosstalk analysis during LPS-induced lung injury. (A)** Schematic illustration depicting the workflow for constructing a reference EC–pericyte crosstalk landscape of a healthy mouse lung. The right panel shows the composition of the cell–cell interaction database. **(B)** Circos plots showing 677 EC–pericyte and 681 pericyte–EC interactions that were identified in healthy lungs. **(C)** Enrichment network analysis of EC–pericyte interactions. **(D)** Volcano plots show the DEGs in ECs and pericytes of LPS-instilled lungs compared with healthy lungs. **(E)** GO biological process analysis of the

DEGs shown in D. Shown are the top five most upregulated and most downregulated pathways in ECs and pericytes. **(F)** Heatmap showing the dysregulated EC–pericyte and pericyte–EC interaction pairs in the lungs of ALI mice compared to healthy controls. **(G)** GO biological process analysis of the LPS-dysregulated EC–pericyte interactions (n = 6 mice per group).

the NO receptor sGC (Evgenov et al., 2006), therefore, *Nos3-Gucy1a1* and *Nos3-Gucy1b1* interactions were designated as eNOS–sGC crosstalk in this study (Fig. 2 B). Analysis of the lung lysates revealed that the eNOS mRNA levels, total eNOS protein levels, and phosphorylation status at Ser 1,177 residue, which reflects eNOS enzymatic activity, were not altered in the lung ECs upon LPS instillation (Fig. 2, C–E). By contrast, the mRNA and protein levels of both Gucy1a1 and Gucy1b1 in lung pericytes were significantly reduced after LPS administration, although the decrease of their protein levels was not as fast as their mRNA levels (Fig. 2, C–G). These data demonstrate that the reduction in *Nos3-Gucy1a1* and *Nos3-Gucy1b1* interaction scores in LPS-instilled lungs is driven by the decreased expression of Gucy1a1 and Gucy1b1.

The role of sGC in regulating vSMCs relaxation and vascular tone has been extensively studied (Stasch et al., 2011). In contrast, only a few studies have reported on the expression of sGC in pericytes in the brain, retina, muscle, and liver (Bettaga et al., 2015; Fukutani et al., 2009; He et al., 2016; Theilig et al., 2001; Yang et al., 2021). In particular, little is known regarding the function of sGC in pericytes. Therefore, we first validated the sGC expression pattern in the lung using *Gucy1a1-EGFP* transgenic reporter mice and GUCY1A1 antibody. Immunostaining results showed that the EGFP signal was completely colocalized with GUCY1A1 antibody staining, indicating that EGFP expression of *Gucy1a1-EGFP* mice faithfully recapitulates endogenous GUCY1A1 expression (Fig. 2 H). Importantly, EGFP-positive cells in the lungs of Gucy1a1-EGFP reporter mice showed typical pericyte morphology, with a large cell body and multiple extended cytoplasmic processes wrapped around the CD31-positive capillary endothelium (Fig. 2 I). In addition, the EGFP-positive cells in the lungs expressed the pericyte-specific markers NG2, Desmin, and PDGFRβ (Fig. 2 J); these cells did not express either the type-I alveolar epithelial cell markers AQUAPORIN-5 and PODOPLANIN or the type-II alveolar epithelial cell marker SFTPC (Fig. S2 A).

Further analysis of Gucy1a1-EGFP mice demonstrated that EGFP was also expressed by pericytes in heart, muscle, liver, kidney, and skin tissue (Fig. S2 B). Unexpectedly, we found that EGFP was expressed at low levels in α-smooth muscle actin (α-SMA)–positive vSMCs in the lungs (Fig. S2 C). To determine the sGC expression levels precisely, we isolated pericytes (EGFP^{high}) and vSMCs (tdtomato^{+}EGFP^{low}) from the lungs of *Gucy1a1-EGFP::Sm22a-CreER^{T2}::Rosa26-LSL-tdTomato* mice and performed RNA transcriptomic profiling. Analysis showed that the mRNA levels of Gucy1a1 and Gucy1b1 in lung pericytes were ∼10-fold higher than in vSMCs (Fig. S2 D). Further analysis of previously published single-cell RNA expression data (Vanlandewijck et al., 2018) confirmed the differential expression levels of sGC in pericytes and vSMCs (Fig. S2 E). The high expression level of sGC in the pericytes of alveolar capillaries and its dramatic decrease in the lungs of ALI mice suggest that sGC signaling may play an essential role in maintaining vascular homeostasis.

Activating NO–sGC pathway increases vascular integrity and reduces lung injury

Previous studies have shown that sGC activation leads to vSMC relaxation and inhibits vSMC migration and proliferation, thereby promoting vSMC quiescence (Evgenov et al., 2006). Therefore, we hypothesized that pharmacologically activating sGC in pericytes could similarly stabilize pericytes and preserve EC–pericyte interactions, thereby maintaining vascular integrity in LPS-instilled lungs. To effectively activate sGC in lung pericytes, we treated the ALI mice with Riociguat, a clinically approved sGC stimulator for the treatment of pulmonary arterial hypertension (Evgenov et al., 2006; Stasch et al., 2011), 3 h after LPS instillation when sGC protein levels were not significantly reduced (Fig. 2 G and Fig. 3 A). To maximally activated the remaining sGC in lung pericytes, we administered Riociguat at a dose of 20 mg/kg every 9 h (Fig. 3 A). Riociguat alone did not change vascular integrity, as evidenced by the lung weight, Evans blue leakage, and immuno-histological analysis (Fig. S3, A–F). In particular, RNA-seq analysis of the whole lung lysates demonstrated that Riociguat treatment in healthy mice impacts only a few genes' expression (15 upregulated and 9 downregulated; Fig. S3, G and H). In contrast, LPS instillation caused massive gene expression alterations (1,005 upregulated and 945 downregulated; Fig. 3 I). Given that LPS treatment causes hypotension in mice (Ehrentraut et al., 2007; Weinberg et al., 1992), we further tested whether Riociguat treatment in LPS-administered mice would develop severe hypotension. Notably, we found that Riociguat treatment only mildly reduced the blood pressure of LPS-treated mice (Fig. S3 I). Therefore, Riociguat treatment at a dose of 20 mg/kg is safe and well tolerated and was used in this study.

We next investigated the therapeutic effects of Riociguat on ALI. Intratracheal LPS instillation strongly induced vascular permeability and lung edema (Fig. 3, B and C). Strikingly, the post-injury administration of Riociguat significantly reduced the amount of leaked Evans blue and the lung weight compared to the LPS-treated group (Fig. 3, B and C). Concomitantly, histological analysis revealed that LPS-induced alveolar septum thickening and the infiltration of erythrocytes (Ter119^{+}) and myeloid cells (Gr1^{+}) were inhibited by Riociguat treatment (Fig. 3, D–F). Flow cytometry analysis of the lung tissues and bronchoalveolar lavage fluid further confirmed that the LPS-induced massive infiltration of immune cells, including neutrophils and monocytes, was diminished by Riociguat treatment (Fig. 3, G and H). Overall, the data demonstrate that the activation of eNOS–sGC signaling by Riociguat potently promotes vascular integrity and alleviates lung injury.

To better understand molecular changes in the lungs upon Riociguat treatment, we performed genome-wide transcriptome profiling of whole-lung lysates of mice treated with PBS, LPS, and LPS + Riociguat. The analysis of DEGs revealed that 1,005 genes were upregulated (Cluster 1) and 945 genes were

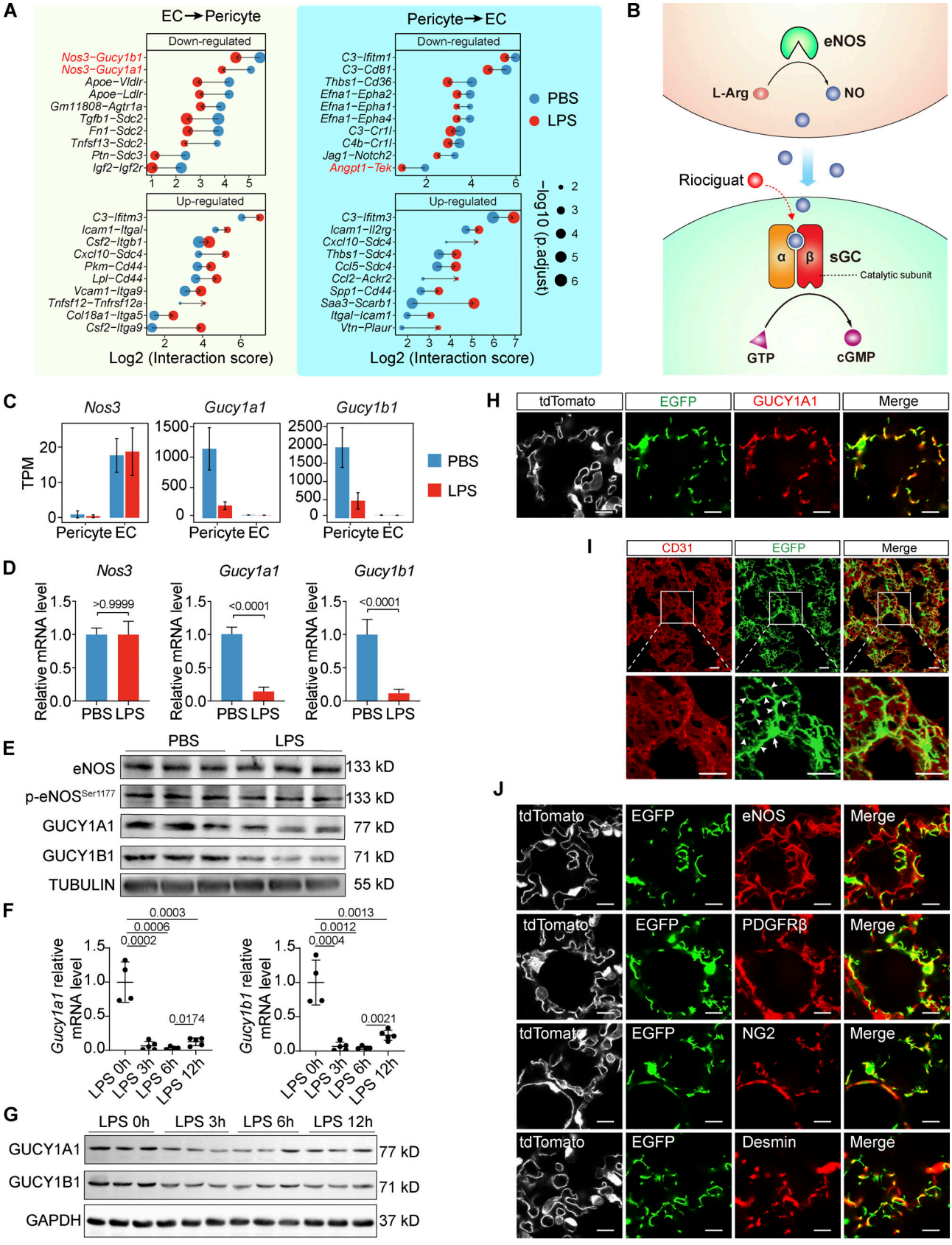

Figure 2. **eNOS–sGC is the most significantly downregulated EC–pericyte interaction in the lungs of ALI mice. (A)** Plot showing the top 10 most significantly upregulated and the top 10 most significantly downregulated EC–pericyte interactions after LPS treatment. The dot size reflects the adjusted P value. **(B)** Schematic diagram showing the intercellular eNOS-NO–sGC signaling. **(C)** Plot showing the TPM values of *Nos3*, *Gucy1a1*, and *Gucy1b1* in ECs and

pericytes isolated from control and LPS-treated lungs. Data are presented as mean ± SD, *n* = 6 mice per group. **(D)** qPCR validation of *Nos3*, *Gucy1a1*, and *Gucy1b1* expression in the lung of control and ALI mice. Data are presented as mean ± SD, *n* = 4–5 mice per group. **(E)** Protein levels of eNOS, p-eNOS^{Ser1177}, GUCY1A1, and GUCY1B1 in PBS- or LPS-treated lungs were analyzed with immunoblotting. **(F)** The kinetics of Gucy1a1 and Gucy1b1 mRNA levels in LPS-instilled lungs was measured using qPCR. Data are presented as mean ± SD, *n* = 4–5 mice per group. **(G)** Protein levels of GUCY1A1 and GUCY1B1 in the lungs after LPS instillation at the indicated time were evaluated using immunoblotting. **(H)** Lung sections of *Gucy1a1-EGFP::Tek-Cre::Rosa26-tdTomato mice* were stained with GUCY1A1 antibody, showing that EGFP expression is colocalized with the endogenous GUCY1A1. Scale bar: 10 µm. **(I)** The morphology of EGFP + pericytes in the lung of a *Gucy1a1-EGFP* mouse. The lung is co-stained with CD31 to show the alveolar vasculature. Arrows indicate the cell body and arrowheads indicate pericyte cellular processes. Scale bar: 20 µm. **(J)** Lung sections of Gucy1a1-EGFP::Tek-Cre::Rosa26-tdTomato mice were stained with the vascular-specific marker eNOS and the pericyte-specific markers PDGFRβ, NG2, and Desmin. Scale bar: 10 µm. Statistical significance was determined by two-tailed Student's *t* test (D) or one-way ANOVA with Tukey test (F). Source data are available for this figure: SourceData F2.

downregulated (Cluster 2) in the LPS-injured lungs; the expression of these genes could be rescued by Riociguat administration (Fig. 3 I). Gene ontology (GO) analysis of the Riociguat-suppressed DEGs was highly enriched for leukocyte-mediated immunity, host defense response, cytokine production, and leukocyte migration (Fig. 3 I). Quantitative PCR (qPCR) analysis confirmed that the expression of LPS-induced inflammatory cytokines, including *Cxcl9*, *Ccl2*, *Il1b*, and *Tnfa*, was suppressed by Riociguat treatment (Fig. 3 J). Additionally, the Riociguat-restored DEGs were enriched for microtubule bundle formation and cilium organization (Fig. 3 I), suggesting that Riociguat treatment protects the respiratory tract from inflammation-induced cilium dysfunction (Tilley et al., 2015). Thus, the data demonstrate that pharmacological activation of the NO–sGC pathway by Riociguat provide a marked therapeutic effect by inhibiting vascular leakage and the local inflammatory response in ALI models.

Pericyte sGC is responsible for improved vascular integrity

In addition to pericytes, sGC is expressed in vSMCs and platelets (Zhang et al., 2011). In particular, platelets have been reported to exert a protective role in a mouse model of LPS-induced systemic sepsis (Xiang et al., 2013). To determine which sGC-expressing cells play the central role in controlling vascular integrity, we specifically inactivated sGC in pericytes, vSMCs, or platelets by crossing *Gucy1b1*$^{flox/flox}$ mice, in which the exon 7 and 8 of *Gucy1b1* were flanked by two *loxp* sites (Zhang et al., 2011), with pericyte cell-specific *Cspg4-CreER*^{T2} mice (designated as *sGC*$^{\Delta PC}$), vSMC-specific *SM22a-CreER*^{T2} mice (designated as *sGC*$^{\Delta SMC}$), or platelet-specific *Pf4-Cre* (designated as *sGC*$^{\Delta PL}$) mice to genetically delete the catalytic β1 subunit of sGC (Fig. 4, A and B; and Fig. S4, A and I). Tamoxifen induction in *sGC*$^{\Delta PC}$ mice successfully reduced Gucy1b1 mRNA and protein levels in the lungs (Fig. 4, C and D). Interestingly, the mRNA and protein levels of Gucy1a1 were also downregulated in *sGC*$^{\Delta PC}$ mice (Fig. 4, C and D), possibly resulting from the disruption of a putative sGC signaling-dependent positive transcriptional. We then analyzed the effect of Riociguat treatment in LPS-instilled *sGC*$^{\Delta PC}$ mice and their littermate controls (*sGC*^{Ctr}). Riociguat treatment in *sGC*^{Ctr} mice successfully reduced LPS-induced lung injury, including the leakage of Evans blue, lung edema, and the infiltration of inflammatory cells (Fig. 4, E–K). However, Riociguat treatment in *sGC*$^{\Delta PC}$ mice did not mitigate LPS-induced lung injury, indicating that Riociguat's lung-protective effect depends on pericyte sGC (Fig. 4, E–K).

Next, we evaluated whether inactivating sGC signaling in vSMCs or platelets affects Riociguat's lung-protective effects. As anticipated, Tamoxifen administration in *sGC*$^{\Delta SMC}$ mice successfully deleted *Gucy1b1* and reduced its mRNA expression in vSMCs (Fig. S4 B). However, vSMC-specific sGC inactivation did not affect Riociguat's lung-protective effects. Riociguat treatment potently reduced LPS-induced Evans blue leakage, alveolar septa thickness, and infiltration of inflammatory cells in both *sGC*^{Ctr} and *sGC*$^{\Delta SMC}$ mice (Fig. S4, C–G). Similarly, platelet-specific sGC inactivation did not impede the protective effect of Riociguat in reducing LPS-induced lung injury in *sGC*$^{\Delta PC}$ mice (Fig. S4, H–K). These in vivo data demonstrate that Riociguat-promoted vascular integrity is contributed primarily by pericytes sGC.

We further validated whether activating NO–sGC signaling in pericytes is sufficient for promoting vascular integrity using a reductionist, microfluidic chip–based, lumenized vascular network that contained only ECs and pericytes; this facilitated the exclusion of any potential interference caused by platelets (Fig. 5 A). Human umbilical vein endothelial cells (HUVECs) and human brain vascular pericytes (HBVPs) were co-cultured in the microfluidic chips for 1 wk to allow the formation of a pericyte-covered vascular network prior to the inflammatory challenge (Fig. 5 A). Given the higher expression levels of TNFR1 compared to TLR4, TNFα is more potent than LPS in activating inflammatory response in HBVPs, as evidenced by their ability to induce *CCL2*, *CCL5*, *IL1b*, and *IL6* mRNA expression in pericytes (Fig. 5, B and D). Therefore, we stimulated HBVPs, unlike in vivo models, with TNFα instead of LPS. TNFα stimulation resulted in a dramatic increase in vascular leakage as evidenced by the accumulation of fluorescent microbeads in the extravascular space (Fig. 5, E and F). Concomitantly, we observed marked morphological changes in pericytes, including the loss of elongated cytoplasmic processes and the formation of lamellipodia, indicating that pericytes had acquired a migrative phenotype (Fig. 5 G). In particular, the formation of F-actin in the detached HBVP was dramatically increased (Fig. 5 G, asterisk). In contrast, treatment with 8-Br-cGMP—a stable analog of sGC-produced cGMP, which directly activates NO–sGC-cGMP signaling cascade in pericytes—suppressed pericyte retraction and restricted vascular leakage (Fig. 5, E–G). Indeed, 8-Br-cGMP treatment induced the formation of multiple elongated cytoplasmic processes wrapped around ECs, closely resembling the morphology of quiescent pericytes in the lungs (Fig. 5 G). This microfluidic-based in vitro analysis suggested that activating the NO–sGC

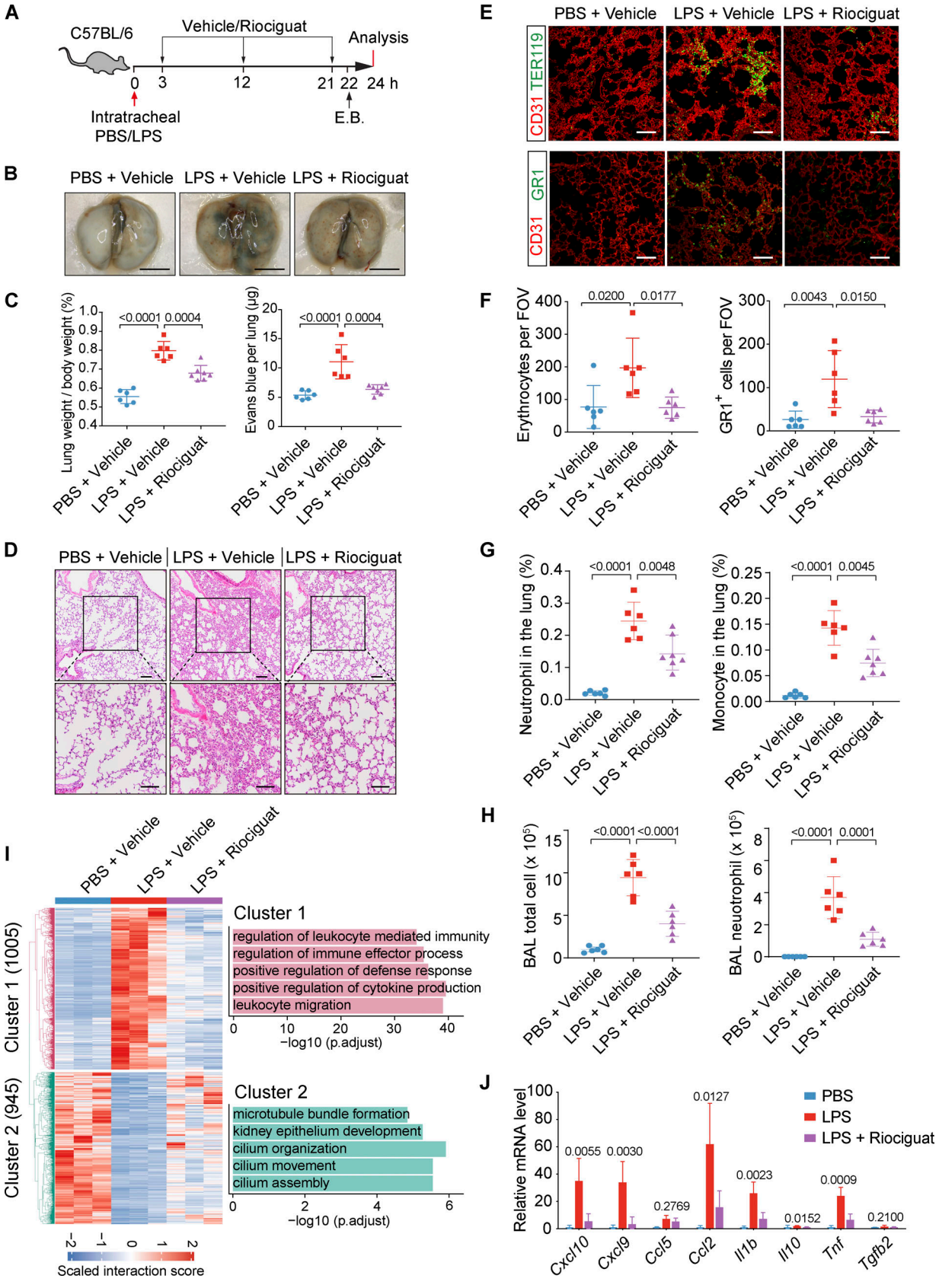

Figure 3. **Activating NO–sGC signaling protects lungs from LPS-induced injury. (A)** Schematic illustration depicting the Riociguat treatment regimen in an ALI model. E.B.: Evans blue. **(B)** Images of the Evans blue–perfused lungs of control, LPS-treated, and LPS + Riociguat–treated mice. Scale bar: 5 mm. **(C)** Quantification of leaked Evans blue in the lungs and the lung weight/body weight ratio. Data are presented as mean ± SD, *n* = 6–7 mice. **(D)** Representative

images of H&E stained lung sections of control, LPS-treated, and LPS + Riociguat–treated mice. The thickening of the alveolar septa was observed in LPS-treated lungs, which was reversed by Riociguat treatment. Scale bar: 100 µm. **(E)** Representative images of Ter119 (erythrocyte), GR1 (neutrophil), and CD31 (EC) stained lung sections. Scale bar: 100 µm. **(F)** Quantification of the extravasated erythrocytes and neutrophils per field of view (FOV). Data are presented as mean ± SD, *n* = 6 mice. **(G)** Plots showing the percentage of infiltrated neutrophils ($CD11b^+Ly6G^+$) and monocytes ($CD11b^+Ly6C^+$) in the lungs of control, LPS-treated, and LPS + Riociguat–treated mice. Data are shown as mean ± SD, *n* = 6–7 mice per group. **(H)** FACS quantification of total infiltrated cells and neutrophils in the bronchoalveolar lavage (BAL) fluid from the lungs of control, LPS-treated, and LPS + Riociguat–treated mice. Data are shown as mean ± SD, *n* = 6–7 mice per group. **(I)** Heatmap showing the DEGs of whole lung lysates from mice treated with PBS, LPS + vehicle, and LPS + Riociguat. The right panel shows the top five enriched GO biological process items. **(J)** qPCR validation of the expression of selected inflammatory cytokines in the whole lung lysates of control, LPS-treated, or LPS + Riociguat–treated mice. Data are presented as mean ± SD, *n* = 3 mice. Statistical significance was determined by one-way ANOVA with Tukey test (C, F, G, H, and J).

pathway in pericytes is sufficient to antagonize inflammation-induced pericyte activation and vascular leakage.

Riociguat treatment suppresses endothelium disruption and pericyte detachment

To reveal the alteration in the alveolar vasculature at the ultrastructural level, we analyzed the lung tissue using transmission electron microscopy (TEM). Increased vascular permeability is usually associated with impaired endothelial tight junctions or aberrant transcytosis (Park-Windhol and D'Amore, 2016). However, TEM analysis revealed that only 0.7% of the alveolar capillaries showed a tight-junction defect upon LPS stimulation. Moreover, this defect was not eliminated upon Riociguat treatment (Fig. 6 A). Further analysis demonstrated that the number of caveolae, which mediate transcytosis, in the alveolar endothelium was also not affected by Riociguat (Fig. 6 B). This was surprising, given the strong protective effect of Riociguat and the prevailing understanding of the importance of tight junctions and transcytosis in controlling vascular permeability. Indeed, the most prominent changes were that the endothelial cytoplasmic membrane of about 25% of alveolar capillaries was mildly disrupted, and 2.3% of alveolar capillaries were severely disrupted upon LPS instillation, which resulted in vascular leakage; however, this endothelial injury was blunted by Riociguat treatment (Fig. 6 C). Interestingly, we also observed pericyte detachment in 1% of the alveolar capillaries in LPS-treated mice, and this detachment was suppressed by Riociguat treatment (Fig. 6 D).

In addition, whole-mount confocal imaging analysis of the *Gucy1a1-EGFP::Tek-Cre::tdTomato* mice, in which the ECs were labeled with tdTomato and pericytes with EGFP, demonstrated that EGFP + pericytes retracted their cytoplasmic processes upon LPS treatment, yielding reduced pericyte coverage. Riociguat treatment inhibited the retraction of pericyte cytoplasmic processes and maintained pericyte coverage (Fig. 6 E). To exclude the possibility that reduced pericyte coverage in *Gucy1a1-EGFP* mice might have resulted from reduced EGFP expression in pericytes after LPS instillation, we further used *Cspg4-CreER^{T2}::Rosa26-LSL-tdTomato* mice, in which the pericytes were permanently labeled with tdTomato upon Tamoxifen induction, to precisely quantify the morphological changes in these pericytes. This analysis demonstrated that LPS instillation induced a significant reduction in both primary and secondary cytoplasmic processes, while Riociguat treatment preserved the cytoplasmic processes wrapped around alveolar capillaries (Fig. 6 F). These data demonstrate that Riociguat treatment antagonizes LPS-induced endothelium breakdown, as well as pericyte retraction and detachment.

Activating sGC signaling suppresses the expression of cytoskeleton arrangement-associated genes in pericytes

To reveal the underlying molecular mechanisms by which NO–sGC signaling promotes vascular integrity, we isolated ECs and pericytes from the lungs of control, LPS-treated, and LPS + Riociguat–treated mice and performed RNA-seq. Both the principal component analysis (PCA; Fig. 7 A) and the number of DEGs (Fig. 7 B) upon Riociguat treatment showed that Riociguat dramatically reversed gene expression in pericytes following the LPS challenge, while it exerted a lesser effect on EC gene expression (594 DEGs in pericytes compared to 195 DEGs in ECs). This finding further substantiated the notion that pericytes are the primary targets of Riociguat. We first analyzed changes in the expression of endothelial junctional molecules. However, RNA-seq revealed that LPS administration induced a heterogeneous response entailing the expression of junctional molecules in ECs. For example, *Cdh5*, *Itgb1*, *and Tjp2* were upregulated, whereas *Cldn5*, *Jam2*, *Jam3*, *Ocln*, *Ptprb*, *Tek*, *and Tjp1* were downregulated following the LPS challenge. More importantly, LPS-induced changes in junctional molecules expression were not reversed by Riociguat, except for *Cldn5*, which was rescued by Riociguat treatment (Fig. 7 C). Along with the TEM results (Fig. 6 A), these data demonstrate that Riociguat has a limited effect on endothelial junctions.

Next, we performed GO analysis of the Riociguat-responsive LPS-regulated genes in pericytes (Cluster_1 of Fig. 7 B) and found that a significant proportion of these genes were enriched for actin and cytoskeleton rearrangement (Fig. 7 D). In addition, gene-set enrichment analysis (GSEA) also confirmed a signature of actin-mediated cell contraction in pericytes after LPS treatment, which was reversed by Riociguat treatment (Fig. 7 E). Subsequent analysis showed that LPS strongly upregulated the expression of cytoskeletal genes, including *Acta2*, *Actg1*, *Rhog*, *Rock2*, *Des*, and *Vim*; this upregulation was reversed by Riociguat treatment (Fig. 7 F).

NO–sGC signaling stabilizes pericyte by suppressing vasodilator-stimulated phosphoprotein (VASP)– and myocardin-related TF A (MRTFA)/serum response factor (SRF)–dependent cytoskeleton rearrangement

To understand how Riociguat suppresses the expression of cytoskeletal genes in pericytes, we performed a transcriptional factor (TF) enrichment analysis and identified SRF as the most

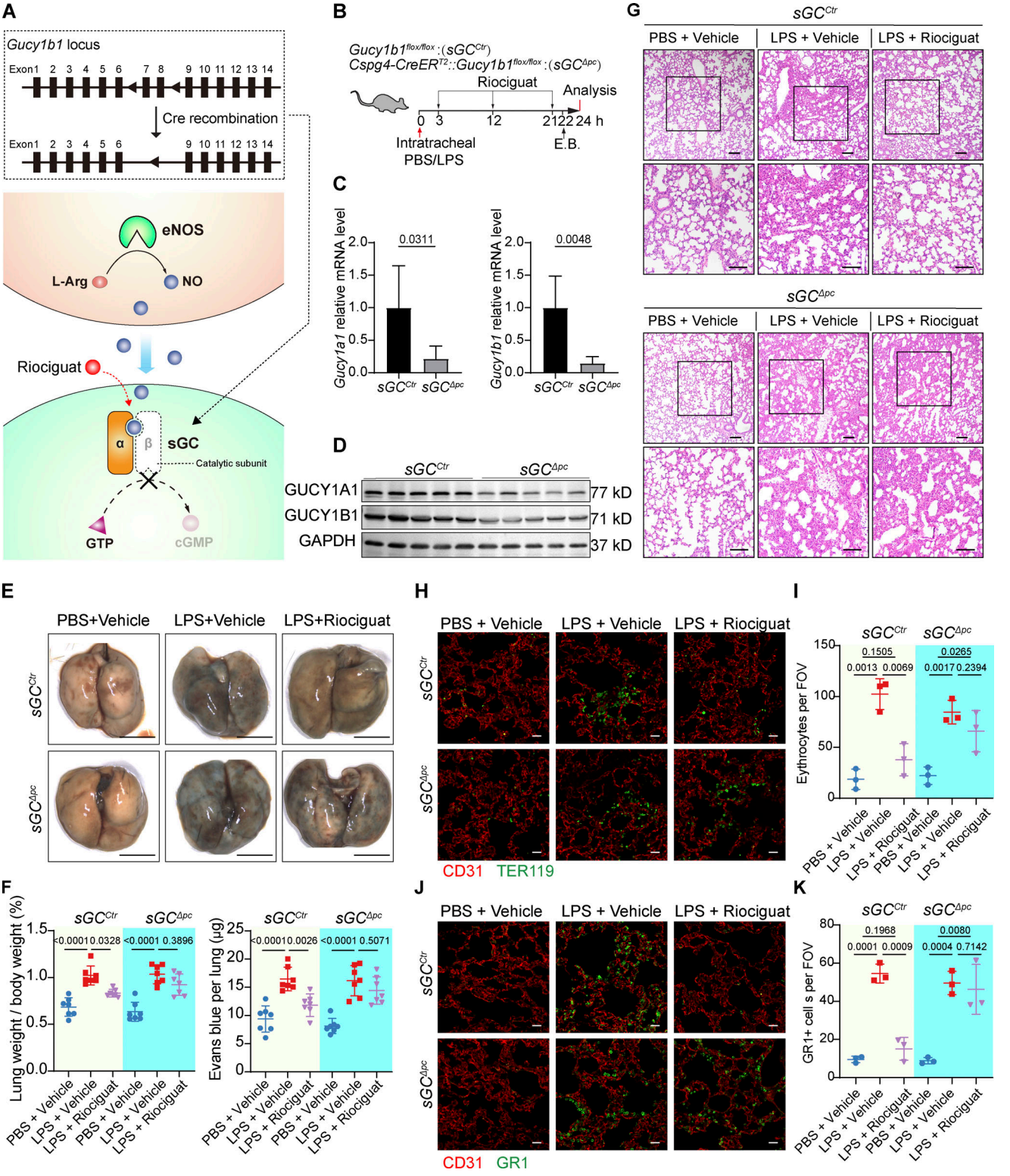

Figure 4. **Pericyte-specific sGC deletion abrogates Riociguat's therapeutic effect. (A)** Schematic diagram depicting the conditional inactivation of sGC signaling by Cre mediated deletion of exon7-8 of *Gucy1b1*. **(B)** Schematic illustration depicting the Riociguat treatment in the PBS/LPS instilled *Gucy1b1*$^{flox/flox}$ (*sGC*^{Ctr}) and *Cspg4-CreER*^{T2}*::Gucy1b1*$^{flox/flox}$ (*sGC*$^{\Delta PC}$, pericyte-specific sGC inactivation). E.B.: Evans blue. **(C)** qPCR validation of the *Gucy1a1* and *Gucy1b1* mRNA levels in the lungs of *sGC*^{Ctr} and *sGC*$^{\Delta PC}$ mice. Data are presented as mean ± SD, *n* = 5 mice per group. **(D)** Western blot of GUCY1A1 and GUCY1B1 protein levels in the lungs of *sGC*^{Ctr} and *sGC*$^{\Delta PC}$ mice. **(E)** Macro images of the lungs of Evans blue–perfused *sGC*^{Ctr} and *sGC*$^{\Delta PC}$ mice treated with PBS, LPS, or LPS + Riociguat. Scale bar: 5 mm. **(F)** Quantification of the amount of leaked Evans blue in the lungs and the lung weight/body weight ratio of *sGC*^{Ctr} and *sGC*$^{\Delta PC}$ mice treated with PBS, LPS, or LPS + Riociguat. Data are presented as mean ± SD, *n* = 7 mice. **(G)** Representative images of H&E stained lung sections of *sGC*^{Ctr} and *sGC*$^{\Delta PC}$ mice treated with PBS, LPS, or LPS + Riociguat. Scale bar: 100 μm. **(H)** Representative fluorescence images showing CD31 and TER119 stained lung sections of

sGC^{Ctr} and sGC$^{\Delta PC}$ mice treated with PBS + vehicle, LPS + vehicle, or LPS + Riociguat. Scale bar: 20 µm. **(I)** Quantification of TER119-positive erythrocytes in the lung section per FOV. Data are presented as mean ± SD, *n* = 3 mice. **(J)** Representative fluorescence images showing CD31 and GR1 stained lung sections of sGC^{Ctr} and sGC$^{\Delta PC}$ mice treated with PBS + vehicle, LPS + vehicle, or LPS + Riociguat. Scale bar: 20 µm. **(K)** Quantification of GR1-positive neutrophils in the lung section per FOV. Data are presented as mean ± SD, *n* = 3 mice. Statistical significance was determined by two-tailed Student's *t* test (C) or one-way ANOVA with Tukey test (F, I, and K). Source data are available for this figure: SourceData F4.

significant upstream regulator (Fig. 8 A) for the genes in Cluster 1 of Fig. 7 B. Analysis of previously published chromatin immunoprecipitation (ChIP) data (Guo et al., 2018) confirmed the binding of SRF to the promoter regions of *Actb*, *Actg1*, *Tpm2*, and other cytoskeletal genes (Fig. 8 B). SRF is a nuclear-localized TF; however, its transcriptional activity and specificity are determined by its coactivator, MRTFA. While MRTFA is normally trapped in the cytoplasm by G-actin under steady-state conditions, inflammatory stimulus induces actin polymerization, which then triggers the dissociation of MRTFA from G-actin. Subsequently, MRTFA translocates to the nucleus and forms an MRTFA/SRF complex to initiate the de novo synthesis of cytoskeletal genes (Gau and Roy, 2018). To confirm whether MRTFA/SRF is an effector of sGC activation, we evaluated the change of MRTFA and SRF subcellular localization in pericytes after inflammatory challenges. Indeed, we found that TNFα stimulation induced the MRTFA translocate from cytoplasm to nucleus (Fig. 8 D), while it did not alter SRF nuclear localization (Fig. 8 C). As expected, activating sGC signaling with 8-Br-cGMP successfully prevented MRTFA nuclear translocation (Fig. 8, D and E). This was further corroborated by in vivo analysis that Riociguat treatment abrogated LPS-induced MRTFA nuclear translocation in the lung pericytes of *Gucy1a1-EGFP* mice (Fig. 8, G and H). Given that MRTFA cytoplasmic sequestration is a consequence of actin polymerization, we evaluated whether NO–sGC signaling controls F-actin formation. Immunofluorescence analysis of F-actin formation using phalloidin staining showed that 8-Br-cGMP treatment abrogated inflammation-induced F-actin polymerization in both 2D (Fig. 8, D and F) and 3D cultured HBVPs (Fig. 5 G). It has been demonstrated that sGC activates downstream cGMP-dependent protein kinase 1 (PKG1; Becker et al., 2000). The activated PKG1 phosphorylates VASP at Ser239, which abrogates VASP-driven actin polymerization in different cell types (Benz et al., 2009; Harbeck et al., 2000). Indeed, activating the sGC–PKG pathway in HBVP using 8-Br-cGMP strongly induced VASP phosphorylation at Ser239 (Fig. 8 J). By contrast, 8-Br-cGMP could not induce VASP(Ser239) phosphorylation in ECs due to a lack of PKG1/2 expression (Fig. 8, J and K). This was further substantiated by immunofluorescence analysis of lung sections demonstrating that Riociguat treatment led to increased p-VASP (Ser329) signal in alveolar pericytes in vivo (Fig. 8 I). Together, these data demonstrate that activation of the sGC-PKG-VASP signaling cascade (either through Riociguat or through 8-Br-cGMP) inhibits F-actin polymerization and suppresses MRTFA nuclear translocation, thereby limiting the SRF/MRTFA-dependent de novo synthesis of factors involved in cytoskeleton rearrangement and eventually stabilizing pericyte.

NO–sGC signaling suppresses pericyte inflammatory responses

Prior research has demonstrated sGC stimulators have been demonstrated to exert anti-inflammatory effects in different disease models (Ahluwalia et al., 2004; Flores-Costa et al., 2020; Hall et al., 2019; Yang et al., 2021; Zimmer et al., 2020). Therefore, we asked whether Riociguat also impacts inflammatory response in lung pericytes. Bioinformatic analysis revealed that, in addition to the cytoskeletal genes, Riociguat also regulated genes that control inflammation and immune cells chemotaxis, including *Il1a*, *Il1b*, *Ccl2*, *Ccl3*, and *Cxcl5* (Fig. 7 D and Fig. S5 A). In line with a previous study indicating that CCL2 is highly expressed in brain pericytes during inflammation to recruit CCR2-expressing monocytes (Duan et al., 2018), CCL2 was induced in lung pericytes upon ALI. Notably, the upregulation of CCL2 in LPS-instilled lungs could be potently suppressed by Riociguat treatment (Fig. S5, B and C). The anti-inflammatory effect of sGC signaling was further validated in cultured HBVPs showing that TNFα stimulation strongly induced CCL2 and IL1b expression in HBVPs, whereas activating sGC signaling by cGMP markedly reduced inflammatory cytokines expression (Fig. S5 D). These results demonstrate the pleiotropic roles of sGC signaling in controlling pericyte function.

Activating NO–sGC signaling partially restores EC–pericyte interactions

Lastly, we analyzed the influence of Riociguat treatment on the LPS-challenged EC–pericyte crosstalk landscape. Differential crosstalk analysis reveals that Riociguat treatment reversed 35% of dysregulated EC→pericyte interaction pairs, and 29% of dysregulated pericyte→EC interaction pairs (Fig. 9 A). Notably, Riociguat treatment elevated *Gucy1a1* and *Gucy1b1* expression in LPS-treated lungs, while it had no effect on *NOS3* expression, resulting in the restoration of *Nos3-Gucy1a1* and *Nos3-Gucy1b1* interactions—which were substantially impaired by LPS (Fig. 9, A–D). These data demonstrate that Riociguat not only promotes vascular integrity but also partially restores EC–pericyte interactions and vascular homeostasis.

Discussion

Increased vascular permeability to fluid and inflammatory cells is the hallmark of ALI. Reducing vascular permeability by manipulating VE-Cadherin, Angiopoietin-2, TIE2, or vascular endothelial protein tyrosine phosphatase has shown promising therapeutic effects in various disease models, including sepsis-induced lung injury (Han et al., 2016; Shen et al., 2014), suggesting that promoting vascular integrity could effectively halt disease progression. In this study, by comparing the lung EC–pericyte crosstalk of healthy and ALI

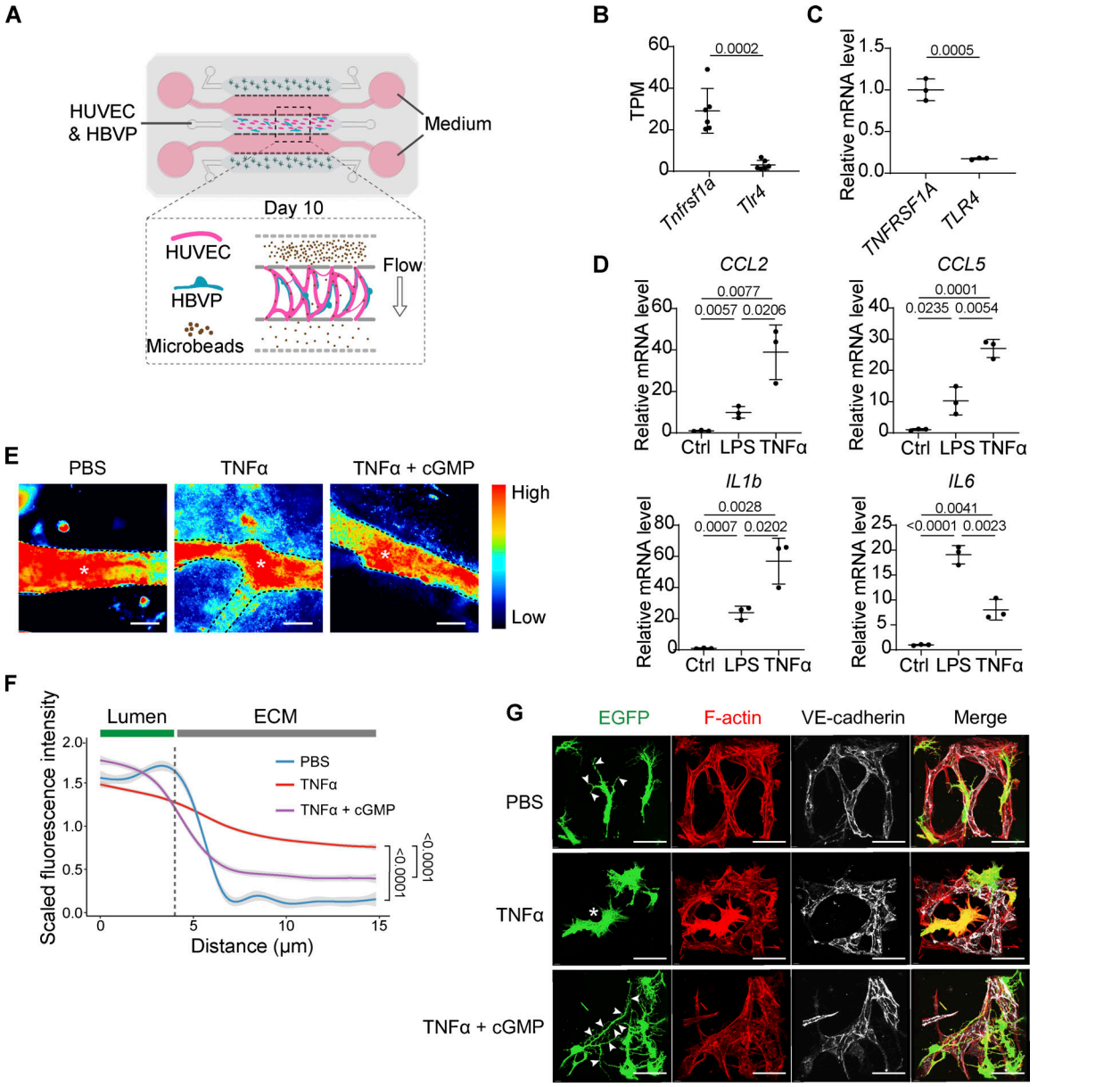

Figure 5. **Activating pericyte sGC signaling improves vascular integrity in vitro. (A)** Schematic illustration depicting the microfluidic chip–based vascular leakage assay. After the vascular network was formed, FITC-microbeads were perfused into the vascular network; the leakage of the FITC-microbeads was monitored and quantified. **(B)** Plot showing the TPM value of Tnfrsf1a and Tlr4 in mouse lung pericytes. Data are presented as mean ± SD, *n* = 6 mice per group. **(C)** qPCR analysis of TNFRSF1A and TLR4 relative expression levels in HBVP. Data are presented as mean ± SD, *n* = 3 biological replicates. **(D)** Dot plots depicting the relative expression levels of *CCL2*, *CCL5*, *IL1b*, and *IL6* in pericytes upon LPS or TNFα treatment. Data are presented as mean ± SD, *n* = 3 biological replicates. **(E)** Representative fluorescent images showing the fluorescence intensity of the leaked FITC-microbeads outside of the capillaries at 30 min after FITC-microbeads perfusion. Scale bar: 20 μm. **(F)** The quantification of FITC fluorescence intensity indicating vascular leakage. The data are shown as a smooth-fitting line with SE (95% confidence interval); *n* = 30 points from 3 chips. Statistical significance was determined using two-way ANOVA. **(G)** Representative images of the lumenized vascular network formed by HUVEC and HBVP (lenti-EGFP–labeled) in microfluidic chips. The pericytes exhibited dramatic morphological changes and detached from the endothelium 48 h after TNFα treatment. 8-Br-cGMP suppressed pericyte TNFα-induced detachment and promoted the formation of pericyte cellular processes. Arrowheads indicate pericyte cellular processes and the asterisk indicates the detached pericyte. Scale bar: 50 μm. Statistical significance was determined by two-tailed Student's *t* test (B and C) or one-way ANOVA with Tukey test (D).

mice, we have found that eNOS-NO–sGC signaling constitutes key EC–pericyte crosstalk that regulates vascular integrity. Post-injury administration of Riociguat activated sGC signaling in lung pericytes, which led to the inhibition of pericyte cytoskeleton rearrangement, thereby abrogating the retraction of cytoplasmic processes and preserving pericyte coverage of the alveolar capillaries. Consequently, Riociguat treatment blunted vascular leakage by stabilizing the vasculature; it also restricted the infiltration of leukocytes. Overall, activating pericyte sGC promoted EC–pericyte interaction, maintained the endothelial barrier, and ameliorated lung injury (Fig. 10).

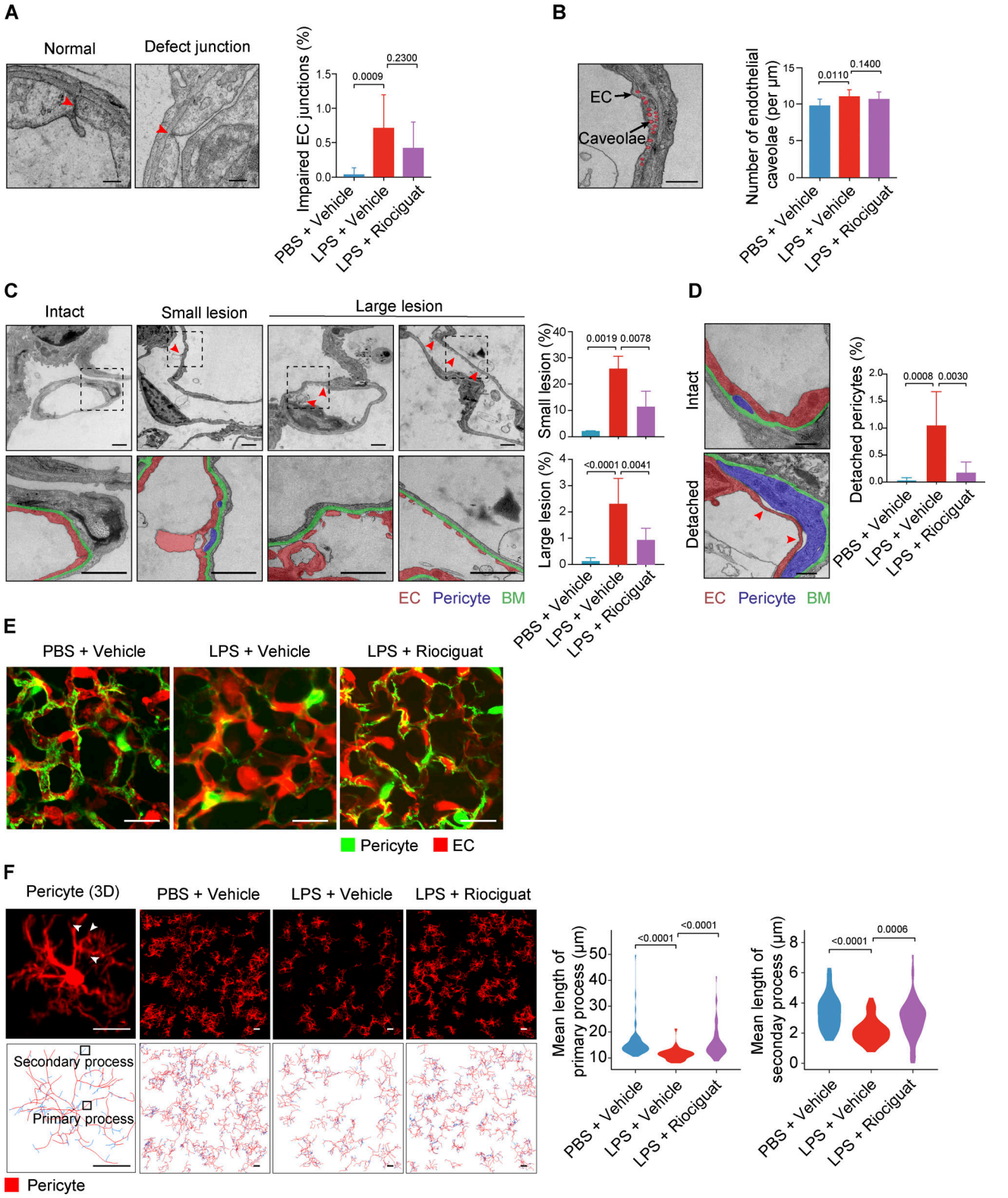

Figure 6. **Morphological analysis of alveolar capillaries. (A)** Representative electron micrographs of intact and impaired endothelial junctions. The percentages of impaired endothelial junctions in the alveolar capillaries of control, LPS-treated, or LPS + Riociguat–treated mice were quantified. Scale bar: 0.5 µm. The data are presented as mean ± SD, *n* = 9 sections from three mice. Statistical significance was determined by the Kruskal–Wallis test. **(B)** Representative electron micrograph of caveolae in alveolar endothelium. The number of endothelial caveolae in the alveolar capillaries of control, LPS-treated, or LPS + Riociguat–treated mice were quantified. Scale bar: 0.5 µm. Data are presented as mean ± SD, *n* = 9 sections from three mice. Statistical significance was determined by the Kruskal–Wallis test. **(C)** Representative electron micrographs of intact and disrupted alveolar endothelium with small or large lesions. Pseudocolors highlight EC (red) and basement membrane (green). Arrowheads indicate the breakdown of the endothelium. Scale bar: 1 µm. Data are presented

as mean ± SD, *n* = 9 sections from three mice. Statistics were performed using the Kruskal–Wallis test. **(D)** Representative electron micrographs showing the normal and detached pericyte cellular process over the endothelium. Pseudocolors highlight EC (red), basement membrane (green), and pericyte (blue). Arrowhead indicate a detached pericyte. Scale bar: 0.5 µm. Data are presented as mean ± SD, *n* = 9 sections from three mice. Statistics were performed using the Kruskal–Wallis test. **(E)** 3D reconstructed images of lung sections of *Gucy1a1-EGFP::Tek-Cre::Rosa26-tdTomato* mice treated with control, LPS, or LPS + Riociguat. Pericytes were labeled with EGFP, and ECs were labeled with tdTomato. Riociguat treatment rescues LPS-induced reduction of pericyte coverage. Scale bar: 5 µm. **(F)** Top panels are representative lung images of sparse-labeled *Cspg4-CreER^{T2}::Rosa26-tdTomato* mice with PBS, LPS, or LPS + Riociguat treatment. Lower panels showing the 3D skeletonized pericytes with primary cytoplasmic processes and secondary cytoplasmic processes coded with red and blue, respectively. Scale bar: 20 µm. Violin plots showing the quantification of the mean length of primary and secondary cellular processes. Riociguat treatment suppressed LPS-induced cellular process retraction. Arrowheads indicate pericyte cytoplasmic processes. *n* = 20–30 sections from three mice. Statistical significance was determined by one-way ANOVA with Tukey test.

Vascular integrity is controlled by both EC and pericytes. However, considerable research over the past decade has investigated the role of individual cell types (either ECs or pericytes) during sepsis and inflammation. Moving beyond single cell-type experiments, we establish the first-ever EC–pericyte crosstalk landscape for both steady-state and ALI lungs. In addition, the expanded cell–cell interaction database is not limited only to the previously described secreted/membrane-anchored ligand–receptor pairs (Ramilowski et al., 2015) but also includes enzyme-small molecule-receptor pairs that were manually curated (refer to the Materials and methods section for further details). Notably, the expanded cell–cell interaction database does not cover all potential signaling pathways mediating cell–cell communication, such as calcium signals transduced through the gap junction. Comparative analysis of WT and ALI lungs reveals bidirectional alterations within the vascular niche (ECs and pericytes) that underlie the progression of ALI. *Nos3-Gucy1a1* and *Nos3-Gucy1b1* were the two most-downregulated EC→Pericyte signaling interactions after intratracheal LPS instillation. sGC, a heterodimer encoded by *Gucy1a1* and *Gucy1b1*, is the only recognized receptor for NO. Upon NO binding, sGC synthesizes cGMP and activates downstream signaling cascades. To stimulate NO–sGC signaling in pericytes, we administered Riociguat—a clinically approved sGC stimulator for treating patients with pulmonary hypertension (Evgenov et al., 2006; Stasch et al., 2011)—to mice after LPS injury. Strikingly, Riociguat treatment restored vascular barrier function by preserving pericyte cytoplasmic processes around the vessels. Although both pericytes and vSMCs in the lung express sGC, the mRNA levels of sGC in pericytes were 10-fold higher than in vSMCs. In addition, pericytes account for 93% of mural cells in the lung, whereas vSMCs accounts for only 7%. In particular, cell type–specific inactivation of sGC demonstrated that SMC-specific deletion of sGC did not impede Riociguat's efficacy in reversing LPS-induced vascular leakage, while pericyte-specific deletion of sGC rendered Riociguat non-effective. Similar to sGC deletion in vSMCs, inactivating sGC in platelets did not affect Riociguat's lung protective effects. Collectively, these data indicate that Riociguat's lung-protective effects are contributed primarily by pericyte sGC.

Complementary in vitro analysis in microfluidic chips demonstrated that directly treating the pericyte-covered vasculature with cGMP potently stabilized pericyte cytoplasmic processes, thus preserving EC–pericyte interaction and maintaining vascular integrity, which suggests that the concentration of intracellular levels of cGMP in pericytes is tightly associated with pericyte function. Intracellular cGMP levels in mural cells can be elevated by either increasing the local NO concentration, promoting sGC-dependent synthesis, or blocking phosphodiesterase-dependent degradation (Schwappacher et al., 2013). However, excessive amounts of NO (either produced by infiltrated leukocytes or the NO donor) may lead to the oxidation of heme in sGC, which inactivates sGC catalytic activity (Evgenov et al., 2006). In addition, the dramatic reduction of sGC expression during ALI suggests that sGC stimulators would potentially be more efficacious than NO donors or phosphodiesterase inhibitors in elevating intracellular cGMP levels and stabilizing pericytes.

Pericyte detachment and concomitant vascular leakage has been observed in many pathological conditions, including systemic and local inflammation (Han et al., 2016), tumor (Morikawa et al., 2002), diabetic retinopathy (Hammes et al., 2004), and metabolically imbalanced brain tissue (Sheikh et al., 2020). We confirmed that inflammation could cause pericyte detachment by inducing the retraction of pericyte cytoplasmic processes in vivo in the LPS-injured lungs and in vitro in the microfluidic chips, using TEM and confocal imaging. The retraction of cytoplasmic processes in pericytes results from cytoskeleton rearrangement, as evidenced by the formation of F-actin and the increased expression of cytoskeletal rearrangement-associated genes upon inflammatory insults. Importantly, these dramatic morphological changes during inflammation-induced pericyte activation can be reversed by stimulating sGC signaling in pericytes. Activated sGC synthesizes large amounts of cGMP, which activates PKG1 in pericytes. Consequently, PKG1 phosphorylates VASP1 at Ser239, which impairs VASP-driven actin polymerization (Benz et al., 2009), thereby keeping the MRTFA–G-Actin complex sequestered in the cytoplasm. Subsequently, the absence of nuclear MRTFA prevents SRF-mediated transcription of cytoskeletal genes (Gau and Roy, 2018).

In addition to the cytoskeleton stabilization effect of Riociguat, transcriptomic profiling of lung pericytes also revealed that activating sGC signaling reduces LPS-induced inflammatory cytokines and chemokines expression such as *Ccl2*, *Il1a*, and *Il1b*. Furthermore, cGMP treatment potently inhibits TNFα-induced *CCL2* and *IL1B* expression in cultured HBVPs. These results are in accord with a recent study showing that activating sGC exerts anti-inflammatory effects in the livers of mice with experimental nonalcoholic steatohepatitis by reducing *Il1b* expression and inflammasome formation (Flores-Costa et al., 2020). However, whether Riociguat's inhibition of inflammatory cytokine

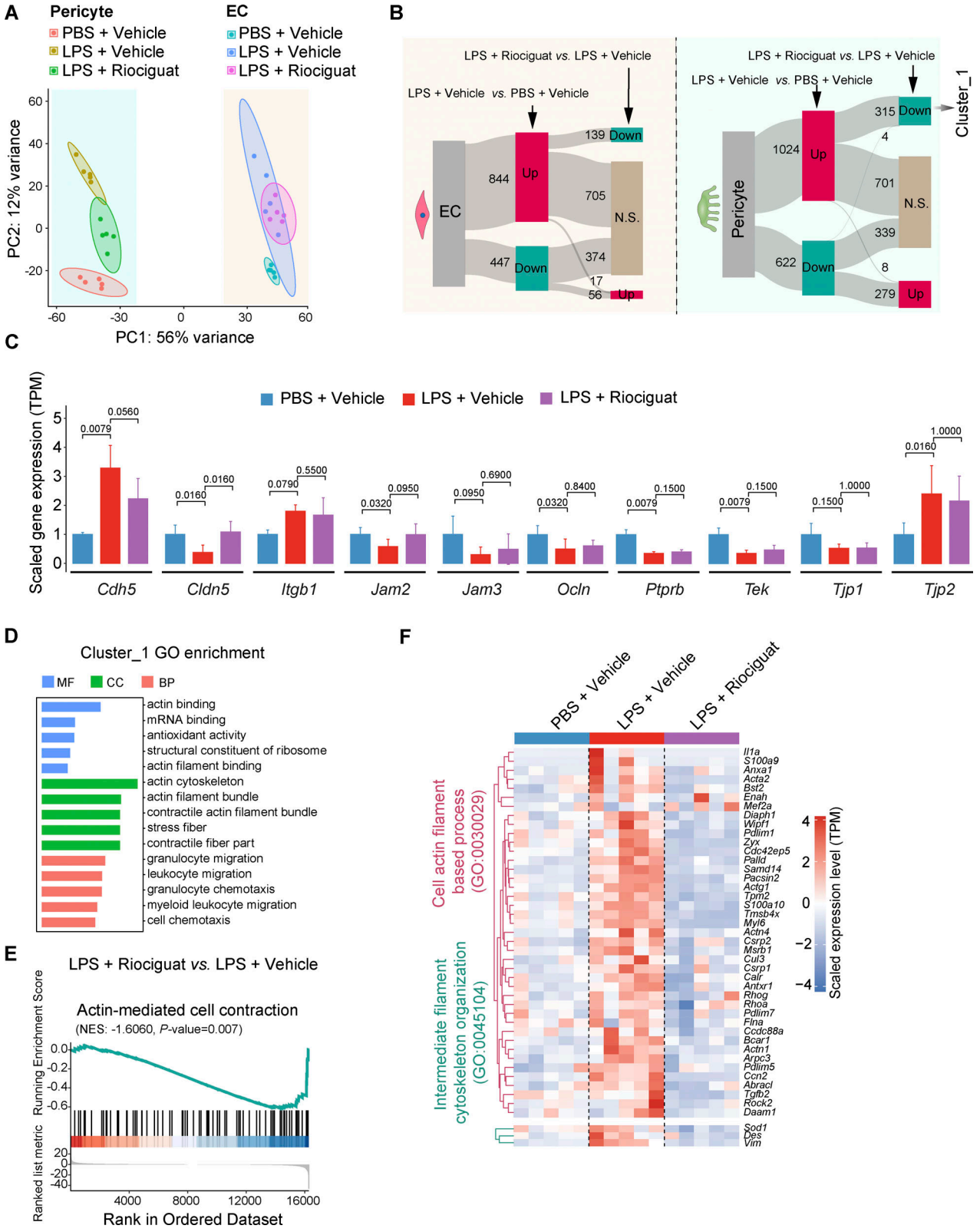

Figure 7. **sGC activation suppresses the expression of cytoskeletal genes in pericytes. (A)** PCA plot of gene expression in the ECs and pericytes of ALI mice showing that Riociguat treatment caused a dramatic gene expression shift in pericytes but not in ECs (n = 5 mice). **(B)** Sankey plot showing the number of DEGs in lung EC upon LPS and LPS + Riociguat treatment (n = 5 mice per group). Sankey plot showing the number of DEGs in lung pericytes upon LPS and LPS + Riociguat treatment (n = 5 mice per group). **(C)** Bar plot shows minor changes of genes involved in endothelial junction formation in the alveolar ECs of PBS + vehicle–, LPS + vehicle–, and LPS + Riociguat–treated mice. Data are presented as mean ± SD, n = 5 mice. Statistical significance was determined by one-way ANOVA with Tukey test. **(D)** GO analysis of the Riociguat-reversed DEGs in pericytes (Cluster_1). Subsets of GO, BP (biological processes), MF (molecular

functions), and CC (cellular components) were used for analysis. The enrichment results were ranked by $-\log_{10}$ (*p*.adjust); only the top 10 items are displayed. **(E)** GSEA reveals that the gene signature of actin-mediated cell contraction in pericytes was upregulated by LPS; this could be suppressed by Riociguat treatment. NES, normalized enrichment score. Genes were pre-ranked by $-\log_{10}$ (*p*.adjust). **(F)** Heatmap showing that Riociguat reversed the expression of LPS-upregulated cytoskeleton rearrangement-associated genes.

synthesis in pericytes is mediated by sGC-induced VASP phosphorylation/cytoskeletal stabilization or other mechanisms awaits further investigation.

Overall, the present study establishes that activating pericyte sGC by Riociguat promotes EC–pericyte interaction, stabilizes alveolar vessels, and protects the lungs from local or systemic inflammation-induced injury. The finding that Riociguat treatment promotes vascular integrity strongly warrants further exploitation to therapeutically interfere with the progression of ALI and other vascular-leakage syndromes, possibly in combination with additional mechanism-driven strategies, including anti-pathogen and anti-inflammatory cytokines.

Materials and methods

Mouse experiments

Gucy1a1-GFP transgenic mice were acquired from GENSAT.org. *Tek-Cre* (Stock No. 008863), *Pf4-Cre* (Stock No. 008535), and *Rosa-tdTomato* (Stock No. 007909) mice were acquired from Jackson Laboratory. The generation of *Cspg4-CreER*^{T2} and *Gucy1b1*$^{flox/flox}$ mice has been described previously (Huang et al., 2014; Zhang et al., 2011). WT C57BL/6N mice were purchased from the Charles River. Because male and female mice may show different inflammatory responses and generate data variability, only male mice were used in this study (Kay et al., 2015). All mice were housed on a 12-h light–dark cycle with free access to food and water in the specific pathogen–free animal facility of the Interdisciplinary Research Center on Biology and Chemistry. All animal experiments were approved by the Institutional Animal Care and Use Committee of the Interdisciplinary Research Center on Biology and Chemistry under permission No. IRCBC-2017-007. All animal experiments were performed in accordance with the Guide for the Care and Use of Laboratory Animals. All primers for genotyping are listed in Table S1.

Cell culture

HUVECs were purchased from PromoCell (C-12208) and cultured in an EC growth medium 2 (PromoCell, C-22011) supplemented with 100 U/ml penicillin and 100 mg/ml streptomycin (15070063; Gibco). HBVP was purchased from ScienceCell (#1200) and cultured in a pericyte medium (#1201; ScienceCell) supplemented with 100 U/ml penicillin and 100 mg/ml streptomycin. Both HUVEC and HBVP were never used after passage 6. Cells were cultured in a 5% CO_2 humidified incubator at 37°C. To examine whether cGMP can inhibit the TNFα-induced inflammatory response, HBVP was seeded at 50,000 cells/ml into a collagen-I (354249m, 0.1 mg/ml; Corning)-coated 24-well plate (CLS3524-100EA; Corning) and cultured for 24 h. HBVP was pre-treated with 50 µM 8-Br-cGMP (B1381; Sigma-Aldrich) for 1 h before TNFα (210-TA-100, 100 ng/ml; R&D) stimulation. In the end, the RNA was extracted for reverse transcription and qPCR analysis.

Intratracheal LPS instillation-induced lung injury model

The mice were anesthetized with isoflurane and fixed in a supine position on a sloped intubating platform. The hair of the surgical area was shaved off and the skin was disinfected with 70% ethanol. The trachea was surgically exposed. Then, the mouse was intratracheally instilled with 50 µl saline or saline containing LPS (2 mg/kg) to induce lung injury. Afterward, the mice were shaken downwards five times to facilitate liquid dispersion. In the end, the skin was closed with a 4/0 suture and the mice were put in the cage for recovery. 24 h later, the mice were euthanized and their lungs were collected and weighed. Then the lungs were fixed in 4% PFA and embedded in paraffin for histology analysis.

Intraperitoneal LPS injection-induced sepsis model

To induce systemic inflammation, 100 µl LPS (6 mg/kg) was intraperitoneally injected into the mice. The first dose of Riociguat was administrated 3 h after LPS injection. Evans blue injection and sample collection were performed just as in the intratracheal LPS injection model described above.

Riociguat treatment regimen

To maximally activate sGC in pericytes, 20 mg/kg Riociguat (S8135; Selleck) was given every 9 h through oral gavage as indicated in Fig. 3 A. The first dose of Riociguat was given 3 h after to LPS instillation. The control group received an equal amount of vehicle. Riociguat stock solution was prepared by dissolving 200 mg Riociguat in 1.5 ml dimethylacetamide. Before oral gavage, the Riociguat solution was freshly prepared by mixing 3 volumes of Riociguat/dimethylacetamide stock with 97 volumes of 20% 2-Hydroxypropyl-β-cyclodextrin/H_2O solution.

Evans blue permeability assay

To evaluate vascular permeability in the lung, 150 µl of Evans blue solution (30 mg/kg, dissolved in saline) was slowly injected into the mice through a tail vein 2 h before sacrifice. Then the mouse was euthanized by an overdose of chloral hydrate (10% in saline) 24 h after LPS administration. The thorax was opened and a cannula was inserted into the right ventricle. Subsequently, the mouse was perfused with EDTA buffer (5 mmol/l EDTA in PBS) at 8 ml/min for 5 min to remove the remaining Evans blue in the pulmonary circulation. Afterward, the lung was carefully dissected and washed with PBS. The lungs were imaged under a Leica stereomicroscope (Leica S6D) mounted with a color camera (Leica MC120 HD). Afterward, the lung was harvested and homogenized. Then the lung lysates were incubated with formamide overnight at 60°C to extract the Evans blue. The max absorption was measured at 610 nm with a microplate reader (SpectraMax i3) and the leaked Evans blue was quantified according to the Evans blue standard curve.

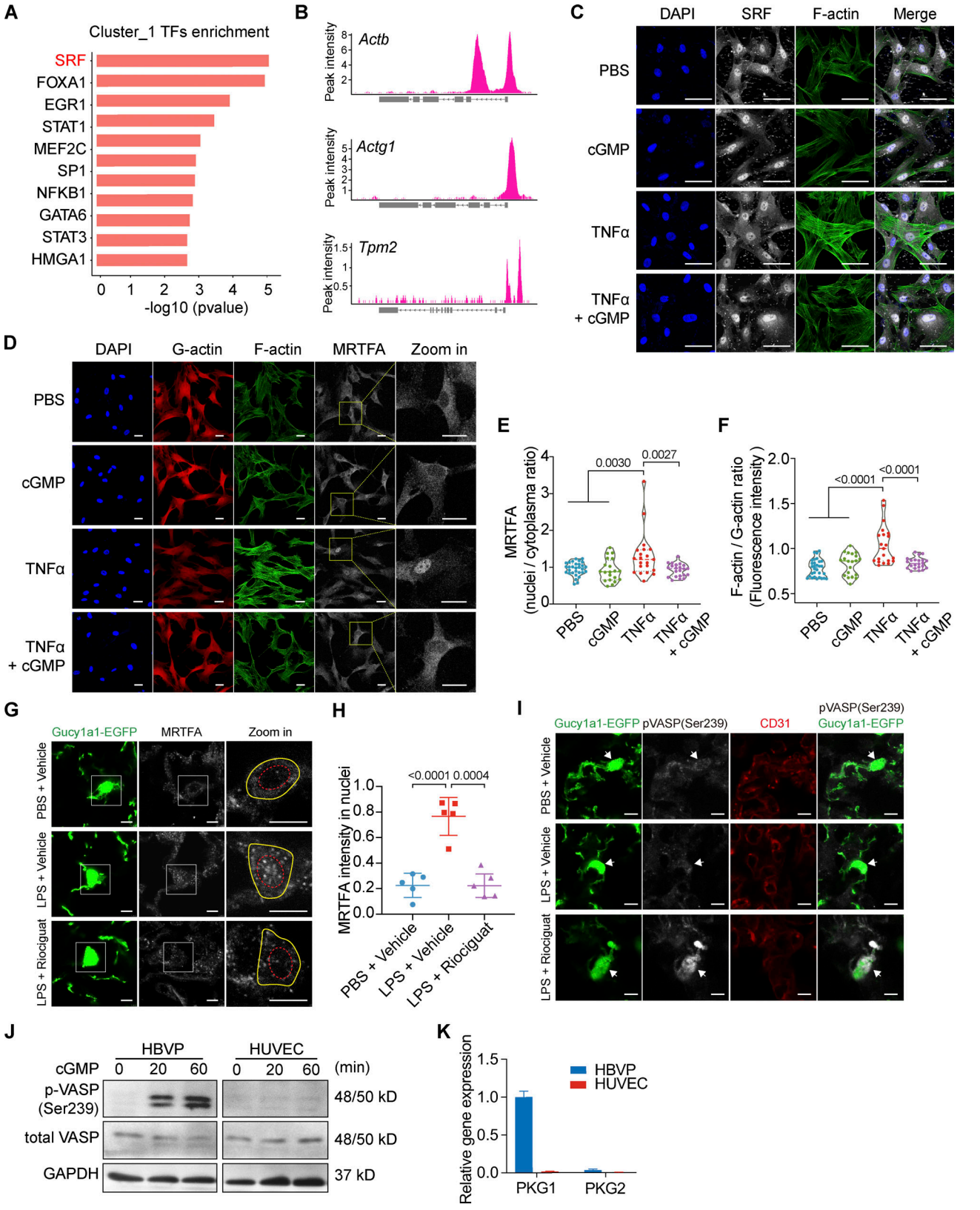

Figure 8. **NO–sGC signaling stabilizes pericyte activation by inhibiting VASP- and MRTFA/SRF-dependent cytoskeleton rearrangement. (A)** Over-representative TF enrichment analysis of genes in Cluster_1 using the TRRUST (v2) database. Only the top 10 TFs are displayed. **(B)** ChIP-seq (SRX3591809) analysis showing the SRF binding site at the promoters of *Actb*, *Actg1*, and *Tpm2*. **(C)** SRF localization in HBVPs upon TNFα or cGMP treatment was evaluated by immunofluorescence staining. Cells were co-stained with DAPI and phalloidin to visualize the nuclei and F-actin. Scale bar: 50 µm. **(D)** HBVPs were treated with vehicle, 8-Br-cGMP, TNFα, or TNFα + 8-Br-cGMP for 30 min. HBVPs were then stained with phalloidin for F-actin and antibodies against G-actin and MRTFA. 8-

Br-cGMP treatment suppressed F-actin assembly and MRTFA nuclear translocation. Scale bar: 25 µm. **(E)** Quantification of the nuclei/plasma MRTFA ratio based on fluorescence intensity. Statistical significance was determined by one-way ANOVA with Tukey test. **(F)** Plot showing the quantification of F-actin/G-actin ratio in HBVPs upon TNFα and 8-Br-cGMP treatment. Statistical significance was determined by one-way ANOVA with Tukey test. **(G)** MRTFA subcellular localization in PBS + vehicle–, LPS + vehicle–, or LPS + Riociguat–treated lungs of *Gucy1a1-EGFP* mice were evaluated using immunofluorescence staining. Scale bar: 5 µm. **(H)** Plot showing the quantification of MRTFA intensity in EGFP + pericyte nuclei of PBS + vehicle–, LPS + vehicle–, or LPS + Riociguat–treated mice. Data are presented as mean ± SD, *n* = 5 mice. Statistical significance was determined by one-way ANOVA with Tukey test. **(I)** VASP phosphorylation status in the lung pericytes of *Gucy1a1-EGFP* mice was evaluated using immunofluorescence staining with a p-VASP(Ser239) antibody. Lung pericytes were labeled with EGFP, and alveolar vessels were stained with CD31. Arrows indicate the cell bodies of GFP-positive pericytes. Scale bar: 5 µm. **(J)** Western blot of total VASP and phospho-VASP (Ser239) in HUVEC and HBVP by 8-Br-cGMP treatment at the indicated time. **(K)** qPCR analysis shows *PKG1* was the downstream effector of activated sGC in HBVPs, whereas HUVECs lack both *PKG1* and *PKG2* expression. Source data are available for this figure: SourceData F8.

Whole-lung lysate transcriptomic profiling

The lungs were snap-frozen in liquid nitrogen and homogenized with TissueLyser II (Qiagen). Total RNA was extracted using the RNeasy mini kit (Qiagen). RNA concentrations were quantified by measuring Abs260 with a NanoDrop 2000c. All RNA-seq libraries were prepared using the VAHTS Stranded mRNA-seq Library Prep Kit for Illumina (Vazyme Biotech Co.; NR-602). Briefly, the polyA fraction (mRNA) was purified using mRNA capture beads from 4 µg of total RNA, followed by fragmentation and generation of double-stranded cDNA. Next, the end repair, dA-tailing, adapter ligation, and PCR amplification steps were performed according to the manufacturer's protocol. The libraries' concentrations were evaluated using a Qubit (Thermo Fisher Scientific) and qPCR (Vazyme Biotech Co.; NQ-103). The length distribution of the cDNA libraries was evaluated using an Agilent Bioanalyzer 2100. Primer dimers were eliminated using Agencourt AMPure XP Bead (A63881; Beckman Coulter) after library preparation. Sequencing libraries were constructed with the VAHTS RNA adaptors set-3 using barcodes to allow multiplexing.

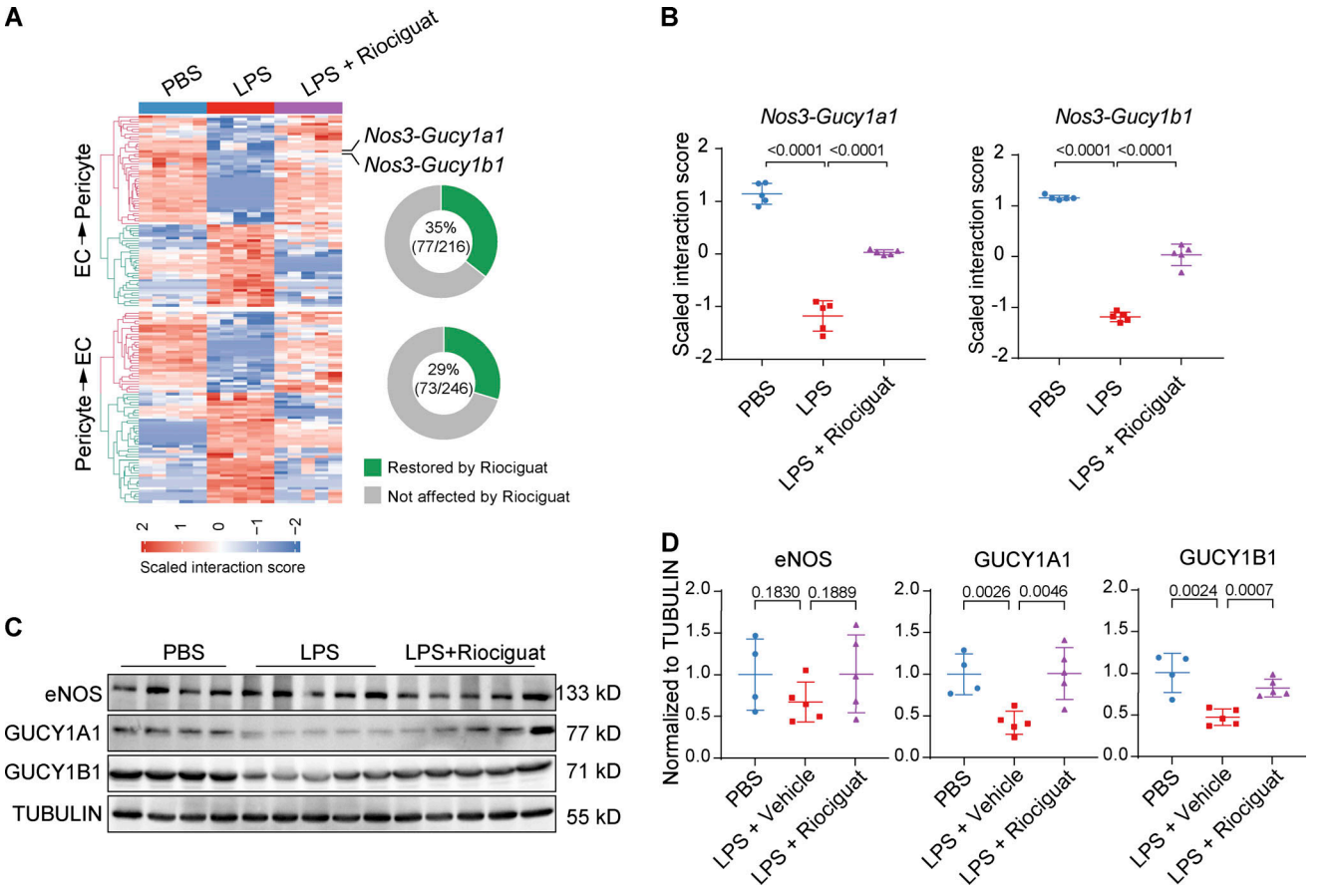

Figure 9. **Activating NO–sGC signaling restores EC–pericyte crosstalk. (A)** Heatmap showing the LPS-dysregulated EC–pericyte interaction pairs that were reversed by Riociguat treatment. Doughnut charts on the right showing the percentage of Riociguat-reversed interactions among the total LPS-dysregulated interaction pairs. **(B)** Plot showing the LPS-dysregulated interactions *Nos3-Gucy1a1* and *Nos3-Gucy1b1* were rescued by Riociguat treatment. Data are presented as mean ± SD, *n* = 5 mice. **(C)** The protein levels of eNOS and GUCY1A1 were validated by Western blot analysis. **(D)** Plots shows the quantification of eNOS, GUCY1A1, and GUCY1B1 normalized to TUBULIN. Data are presented as mean ± SD, *n* = 4–5 mice. Statistical significance was determined by one-way ANOVA with Tukey test. Source data are available for this figure: SourceData F9.

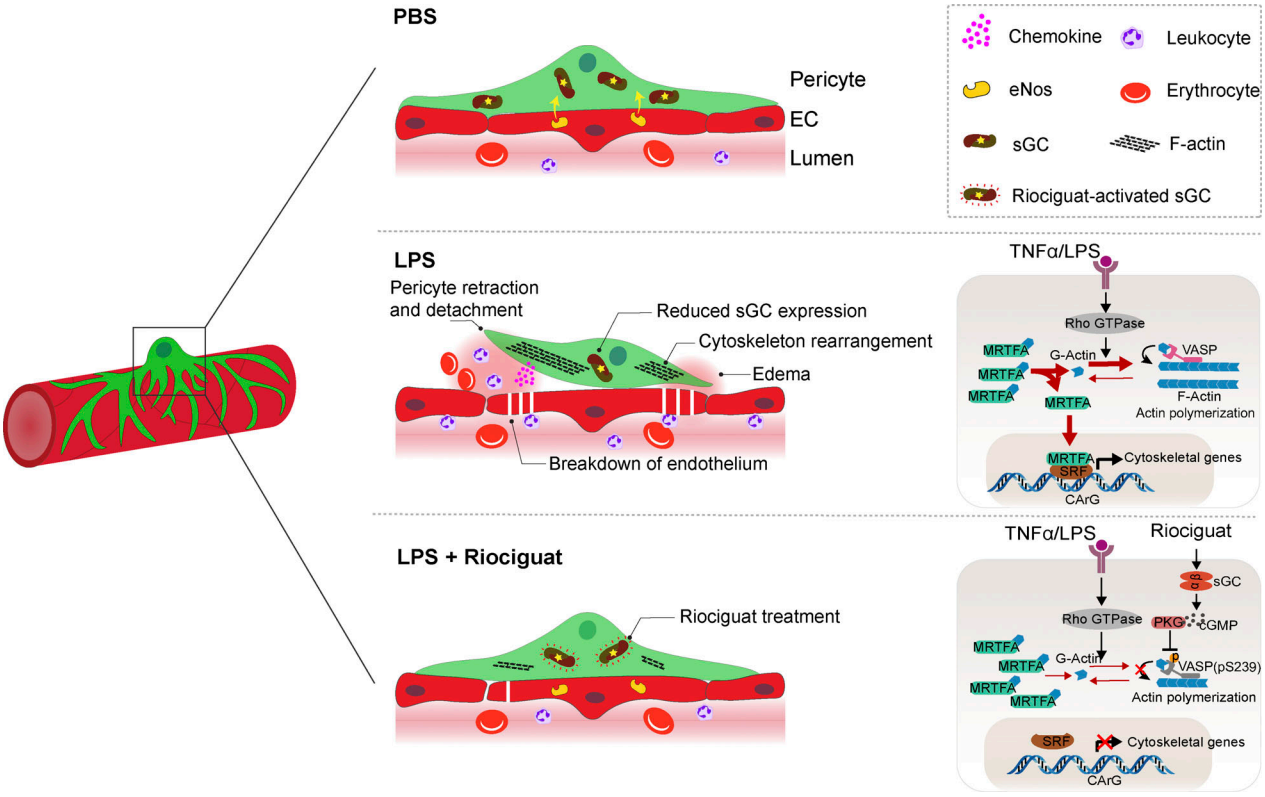

Figure 10. **Working model.** eNOS–sGC signaling, as a key mediator of EC–pericyte crosstalk, controls vascular integrity. In LPS-induced ALI, the eNOS–sGC crosstalk is significantly reduced, resulting in cytoskeleton rearrangement, pericyte detachment, and elevated chemokine expression. This leads to immune cell infiltration, breakdown of the endothelium, and lung edema. Administration of the sGC stimulator Riociguat is sufficient to stabilize EC–pericyte interaction, promoting vascular integrity and reducing inflammation-induced lung injury.

Lung ECs and pericytes isolation and RNA-seq analysis

To isolate lung ECs and pericytes, *Pdgfrb-EGFP* mice or *Gucy1a1-EGFP* mice were euthanized with 10% chloral hydrate. The mice were perfused through right ventricle of the heart with PBS-EDTA (5 mmol/l) buffer at 8 ml/min rate for 5 min. Then the lungs were minced into 1 × 1 mm sizes and were further enzymatically dissociated by incubating with 100 µg/ml Liberase (04942078001; Roche) and 20 µg/ml DNaseI (10104159001; Roche) at 37°C with shaking for 1.5 h. Afterward, the cell suspension was filtered with 70 µm cell strainer (CLS431751; Corning). The cells were first blocked with CD16/CD32 (1:200, 553141; BD) for 5 min at 4°C and then stained with CD31-APC (1:200, 551262; BD), CD45-PE (1:400, 561087; BD), Ter119-PE (1:400, 553673; BD), and Podoplanin-PE (1:200, 12-5381-82; eBioscience) for 30 min at 4°C. Then, 300 lung ECs ($CD31^+/CD45^-/Ter119^-/Podoplanin^-/GFP^-$) or 300 pericytes ($GFP^+/CD31^-/CD45^-/Ter119^-/Podoplanin^-$) were directly sorted (MoFlo Astrios, Beckman Coulter) into 4 µl lysis buffer containing free dNTPs and tailed oligo-dT oligonucleotides. The sequencing library was prepared according to the SMARTseq2 protocol with modifications (Picelli et al., 2014). In brief, the RT reaction was performed with Superscript II reverse transcriptase (18064-014; Invitrogen). Afterward, the cDNA was amplified using KAPA HiFi HotStart ReadyMix (KAPA Biosystems, KK2602). The tagmentation and amplification reactions were completed according to the manufacturer's protocol using the TruePrep DNA Library Prep Kit V2 for Illumina (TD502; Vazyme Biotech Co.). The library purification was then processed with AMPure XP beads (A63881; Beckman Coulter) to eliminate the oligo dimers and large fragments. For each library, the concentration was measured using a Qubit (Thermo Fisher Scientific) and qPCR (NQ-103; Vazyme Biotech Co.); the size distribution was determined using Agilent Bioanalyzer 2100. DNA sequencing was performed using TruSeq dual-index sequencing primers on the Illumina Hiseq 4000 instrument following the 150-bp paired-end sequencing procedure. All sequencing data are available from Gene Expression Omnibus with the accession number GSE162355 and GSE207868.

Bioinformatics

Raw FASTQ files were quality-checked using FASTQC (v0.11.8). All samples had a similar distribution on library size or adapter contamination; no samples were discarded at this step. Then fastp (v0.19.4) was used to quality-trim FASTQ files by both read quality and length (Q30 > 20, length >36). After trimming, clean reads were processed to pseudo-align to mouse transcriptome GRCm38 (Ensembl release 95) using salmon (v0.11.1). The following analysis steps were processed using R/Bioconductor packages. Briefly, transcriptional-level expression was aggregated to gene-level expression using tximport (v1.10.1). The samples' similarity and qualities were checked by mitochondrial counts population analysis, PCA, and sample-to-sample

correlation analysis. Samples were discarded if the percentage of mitochondrial counts was over 5% or if the samples were obvious outliers. We finally included six samples per group for *Pdgfrb-EGFP* mice and five samples per group for *Gucy1a1-EGFP* mice. DEGs were defined by DESeq2 (v1.22.2) with a foldchange ≥1.5 and an adjusted P value <0.05. A DEGs-based hypergeometric test and a GSEA were performed with clusterProfiler (v3.10.1) with default settings, unless otherwise specified. For the GSEA, the ranking metric was calculated as $-\mathrm{Log}_{10}$ (p.adjust).

Expanded cell–cell crosstalk database

The expanded cell–cell crosstalk database was constructed based on the database described by Ramilowski et al. (2015), which only included plasma membrane–bound and secreted ligands, and their cognate membrane-bound receptors (Ramilowski et al., 2015). However, many important intercellular communications are mediated by small molecules and gas molecules, which cannot be directly identified by RNA-seq. To circumvent this, we used RNA-seq data to identity the small-molecule-generating enzyme to infer the presence of signaling molecules. Then, we defined three types of interaction pairs: secreted ligand–receptor, membrane-anchored ligand–receptor, and enzyme-small molecule-receptor. For the first type, we combined ProteinAtlas secretome and UniProt secreted genes to generate secreted genes and searched corresponding receptors through STRING, KEGG, BioGRID, and BIND. For the second type, we used BIND, DIP, STRING, and UniProt to keep pairs whose ligand and receptor were both membrane-bound proteins. For the last type, we inferred enzyme reactions and small molecule–related pairs from BioGRID and KEGG. A confidence score was used extract interaction pairs that were experimentally validated. A high score was given to pairs recorded by various databases or were experimentally validated. For pairs recorded in STRING, additional STRING confidence was also scaled and added. We then filtered the raw database and merged it with the original cell–cell interaction database. Finally, all interaction pairs in the database were manually curated and all pair names were converted to gene's official symbols using the biomaRt R/Bioconductor package.

Cell–cell interaction analysis

We used normalized TPM values instead of the cap analysis of gene expression value used by Ramilowski et al. (2015) to calculate the gene expression levels (Ramilowski et al., 2015). Because of RNA sequencing noise, only genes with a TPM ≥ 2 were considered to be expressed and thus processed for further calculation. The interaction score was calculated as $\sqrt{(ligandTPM)^2 + (receptorTPM)^2}$. The putative cell–cell interaction was displayed as circos plots rendered by the ggraph R package with edge bundling (tension = 0.5). For differentially changed interaction analysis upon LPS and Riociguat treatment, the two-tailed Wilcoxon signed-rank test was used to calculate the significance and the P values were adjusted using the Benjamini–Hochberg multi-comparison correction method.

Immunofluorescent staining sample preparation

For general mice lung imaging, lung alveoli were inflated with 600 µl 4% PFA and tracheae were tied up. The lungs were then fixed by immersion in 4% PFA to prevent the collapse of alveolar sacs. After 24 h of fixation, the lungs were rinsed with PBS; then any adherent fat tissue was carefully removed. Frozen sections of the lung were prepared using a cryostat (4583; Leica). Five sets of 20-µm-thick serial sections were prepared from each lung. The serial section sets were 200 µm apart. For mice lung 3D imaging, lung fixation procedures were the same as above. After fixation, 2-mm-thick lung sections were cut off using surgical blades and preserved in cryo-protection solution for further analysis.

Immunofluorescent staining and imaging

Cryosections were rinsed with PBS and subsequently permeabilized and immuno-blocked for 1 h at room temperature with 10% donkey serum (935; Absin), 1% BSA (A600332; Sangon), and 0.5% Triton-X100. Primary antibodies diluted in 5% donkey serum were incubated overnight at 4°C. After three times washing (30 min each time), secondary antibodies diluted in 5% donkey serum were incubated for 1 h at room temperature. After another three times washing, sections were mounted using ProLong mounting medium (P36961; Invitrogen). Images were acquired through confocal microscopy equipped with a 10×/63×/100× objective lens (SP8; Leica). For 3D whole-mount imaging, a tissue clearing step was performed instead of mounting. We used RapiClear 1.52 (RC152001; Sunjun Lab Co) to clear lung sections for 1 h at room temperature just before imaging. The cleared tissues, placed on a thin-bottom µ-slide (80826; Ibidi), were imaged with spinning-disk confocal microscopy equipped with 10×/40×/63× objective lens (Nikon). Antibodies used in this study were mouse anti-eNOS (ab76198, 1:400; Abcam), rabbit anti-PDGFRβ (MA5-15143, 1:100; Thermo Fisher Scientific), rabbit anti-NG2 (ab129051, 1:100); Abcam, rabbit anti-Desmin (Ab15200-1, 1:400; Abcam), rat anti-TER119 (557915, 1:400; Abcam), rat anti-GR1 (108419, 1:200; Biolegend), Hamster Armenia anti-CD31 (MA3105, 1:200; Thermo Fisher Scientific), rabbit anti-GUCY1A1 (12605-1-AP, 1:200; Proteintech), rabbit anti-SFTPC (PA5-71680, 1:200; Invitrogen), rabbit anti-Podoplanin (14-5381-82, 1:100; Invitrogen), rabbit anti-AQUAPORIN5 (ab78486, 1:200; Abcam), mouse anti-SMA (C6198, 1:200; Sigma-Aldrich), rabbit anti-CLAUDIN5 (ab15106, 1:200; Abcam).

Pericyte-, vSMC-, or platelet-specific *Gucy1b1* deletion

To delete *Gucy1b1* in pericytes, vSMCs, or platelets, we first crossed *Gucy1b1*$^{flox/flox}$ mice with pericyte-specific *Cspg4-CreER*^{T2} mice, *SM22a-CreER*^{T2} mice, or *Pf4-Cre* mice, respectively. To induce the excision of *Gucy1b1* alleles, *Cspg4-CreER*^{T2}::*Gucy1b1*$^{flox/flox}$ (*sGC*$^{\Delta PC}$), *SM22a-CreER*^{T2}::*Gucy1b1*$^{flox/flox}$ (*sGC*$^{\Delta SMC}$), and *Pf4-Cre*::*Gucy1b1*$^{flox/flox}$ (*sGC*$^{\Delta Pl}$) mice were intraperitoneally injected with Tamoxifen (100 µl, concentration 20 mg/ml of peanut oil, T5648; Sigma-Aldrich) for 5 consecutive days at age of 4 wk old. In parallel, their littermates control *Gucy1b1*$^{flox/flox}$ (*sGC*^{Ctr}) also received same amount Tamoxifen injection. Lung injury were

induced by LPS instillation at age of 8 wk. The Gucy1b1 deletion efficiency were evaluated using qPCR and Western blot.

In vivo sparse-labeling pericytes morphology analysis

To precisely analyze the pericyte morphological changes upon LPS or Riociguat treatment, we administered the *Cspg4-CreER^{T2}::Rosa26-tdTomato* mice with low-dose Tamoxifen (25 mg/kg, single injection) by intraperitoneal injection at age of 4 wk. Then the mice were instilled with PBS or LPS at age of 8 wk. 3D whole-mount lung imaging and 3D microfluidic chip imaging were used to analyze pericyte morphology. Images were first imported into Bitplane Imaris software (7.2) and subsequently down-sampled to 512 × 512 pixels for fast computing. The morphology analysis was implemented by filament module on the pericytes fluorescence channel. Primary processes were defined by "branch" and secondary processes were defined by "spine." The software parameters were fine-tuned carefully to match visual inspection. When comparing differences, the same parameter setting was applied for all conditions. After computing analysis, the detailed results were exported. Further statistics and plots were performed by R/Bioconductor packages.

TEM

The lung was first perfused with cold PBS with 5 mmol/l EDTA and then perfused with 20 ml cold 4% PFA. We further inflated the alveolar space with 700 µl cold 4% PFA, tied up the trachea, and continued to fix whole lungs by immersing them into 4% PFA for 3 h. After PFA fixation, we cut off several 1 × 1 mm cubes using a sharp scalpel and then changed the fixation reagent to 2.5% glutaraldehyde solution and fixed the samples overnight. The remaining transmission electron microscopy sample-preparation procedures were conducted following facility-provided instructions. We took the best-fixed cube to the final section preparation and imaging. Acquired images were manually labeled to specify endothelial cells, base membrane, pericytes, tight junctions, and disrupted spots. The detached pericytes, impaired tight junctions, or the breakdown of endothelium were quantified in FIJI.

Microfluidic chip assay

Microfluidic chips were designed and fabricated according to the previous study (Kim et al., 2013). In brief, HUVEC and HBVP were trypsinized and resuspended in 5 mg/ml fibrinogen (F8630; Sigma-Aldrich), supplemented with 10 µM Ilomastat (HY-15768; MCE) at a density of 16E6 cell/ml (HUVEC) and 2E6 cell/ml (HBVP). The 2× mixture was then mixed with 2 U/ml thrombin (T4648; Sigma-Aldrich) at a 1:1 (vol:vol) ratio. To reduce dye diffusion into fibrin gel, the medium sides of the middle fibrin HUVEC/HBVP channel were coated with HUVEC monolayer by filling 1E5 HUVEC and then tilting the chip vertically. Chips were then placed in a humid chamber and given fresh endothelial growth medium 2 every 2 d. At day 8, the formed vessels tended to be mature (well-perfusable and less remodeling). We added 100 ng/ml TNFα or TNFα + 50 µM 8-Br-cGMP to the medium for an additional 2 d. At day 10, cells were fixed by introducing 4% PFA into the medium channel for 6 h. Then, the staining procedures described above were followed.

For fluidic-based leakage assay, chips were placed on an inverted microscopy (with humid CO_2 culturing thermo chamber). The channel medium was aspirated away and 0.01% 100 nm FITC-conjugated microbeads (GF100C; Hugebio) were introduced from one side of the channel and flowed into the vessel due to the altitude difference. Images were acquired at 2-min intervals. The leakage evaluation was processed in FIJI by profiling the fluorescence intensity from the vessel wall lumen side to the extracellular matrix side. Fluorescence intensity was scaled within a single measurement. Smooth curves were then fitted using the locally weighted scatterplot smoothing method. The fluorescence intensity ratio of the extracellular matrix and vessel lumen was used for statistics.

Lung lysate CCL2 ELISA analysis

The adherent connective tissue and adipose tissue were removed from the lungs and then quickly snap-frozen in liquid nitrogen and homogenized with the TissueLyser II (Qiagen). Total protein was extracted using modest protein lysis buffer (P0013F; Beyotime) with a protease inhibitor cocktail (1:100, B14001; Sangon) and phosphatase inhibitor cocktail (1:100, B15001; Sangon). After centrifugation, the supernatant protein concentration was measured using the BCA protein quantification kit (20201ES76; Yeason). All of the samples were then adjusted to the same concentration and further diluted to 50 µg/ml. The lysate CCL2 protein level was quantified using an ELISA kit (PC125; Beyotime) and all of the subsequent procedures were performed according to the manufacturer's instructions.

Western blot

For lung tissue, lungs were snap-frozen in liquid nitrogen and homogenized with a TissueLyser II (Qiagen) by adding 400 µl radioimmunoprecipitation assay buffer with a protease inhibitor cocktail (1:100, B14001; Sangon) and a phosphatase inhibitor cocktail (1:100, B15001; Sangon). For culturing cells, the medium was aspirated and a radioimmunoprecipitation assay buffer with a protease inhibitor cocktail (1:100, B14001; Sangon) and a phosphatase inhibitor cocktail (1:100, B15001; Sangon) was added. After incubation, the lysate was centrifuged and the supernatant protein concentration was measured using the Bicinchoninic Acid Assay protein quantification kit (20201ES76; Yeason). The protein was then supplied with a 3× loading buffer (6% β-mercaptoethanol added) and boiled for 10 min at 90°C; it was then stored at −80°C for further use. Proteins were separated by 10% SDS-PAGE gel, then transferred to nitrocellulose membranes through semi-dry transferring (BioRad, Tans-Blot Turbo system). The transfer efficiency was checked by Ponceau S staining. Then membranes were blocked with 5% BSA for 30 min at room temperature and incubated with primary antibodies at 4°C for 16 h. After washing three times with TBS-T (0.05% Tween-20), the second antibodies were incubated for 1 h at room temperature. After washing three times with TBS-T, enhanced chemiluminescence substrate was added to visualize bands, which were recorded by a chemiluminescence imager (GE AI 6000). Antibodies used were rabbit anti-GUCY1A1 (12605-1-AP, 1:1,000; Proteintech), rabbit anti-GUCY1B1 (ab154841, 1:1,000; Abcam), mouse anti-GAPDH (HC301-02, 1:

2,000; TransGen), mouse anti-eNOS (ab76198, 1:1,000; Abcam), rabbit anti-p-eNOS$^{(Ser1177)}$ (PA5-97371, 1:1,000; Thermo Fisher Scientific), rabbit anti-VASP (3132S, 1:1,000; Cell Signaling Technology), rabbit anti-p-VASP$^{(Ser239)}$ (3114S, 1:1,000; Cell Signaling Technology), mouse anti-Tubulin (HC-101-01, 1:10,000; Transgenbiotech), HRP-conjugated donkey anti-rabbit (711-036-152, 1:2,000; Jackson), HRP-conjugated donkey anti-mouse (715-036-151, 1:2,000; Jackson).

qPCR analysis

The lungs were snap-frozen in liquid nitrogen and homogenized with TissueLyser II (Qiagen). The culturing cells were lysed directly by Trizol (15596026; Invitrogen). Total RNA was extracted using the RNeasy mini kit (217004; Qiagen) and transcribed into cDNA using the ReverTra Ace qPCR RT Master Mix (FSQ-301; Toyobo). qPCR was performed with self-designed primers and PowerUp SYBR Green Master Mix (A25778; Invitrogen) on a QuantStudio 5 system (Thermo Fisher Scientific). Gene expression levels were calculated based on the Delta-Delta Ct relative quantification method. The primers for qPCR used in this study are listed in Table S2.

Statistical analysis

For two-group comparison, non-parameter unpaired Student's *t* tests or the Wilcoxon Signed Rank Test were used. One-way ANOVA or the Kruskal–Wallis test with a Benjamini–Hochberg multi-test correction was used for multiple groups comparisons. Normality was validated by the Shapiro-Wilk test. Analyses were performed by the GraphPad Prism 7 Software or R/Bioconductor. A P value (for two groups) or adjusted P value (for three or more groups) <0.05 was considered to be statistically significant. All data are presented as the mean ± SD unless otherwise specified. The number of animals represents biological replicates and is displayed as a dot number, unless otherwise specified.

Online supplemental material

Fig. S1 shows the strategy for EC and pericyte isolation, cell purity analysis, and RNA-seq analysis of isolated cells from the lungs of healthy and LPS-instilled *Pdgfrb-EGFP* mice. Fig. S2 shows the expression pattern of Gucy1a1-EGFP in pericytes of different organs and the expression levels of sGC in pericytes than vSMCs. Fig. S3 shows Riociguat alone did not change vascular integrity in healthy mice. Fig. S4 shows vSMCs- or platelet-specific sGC inactivation does not abolish Riociguat's lung protection effects in ALI model. Fig. S5 shows Riociguat suppresses LPS-induced inflammatory cytokine expression in lung pericytes in vivo and 8-Br-cGMP inhibits TNFα-induced inflammatory cytokine expression in HBVP in vitro. Table S1 lists the primers for genotyping and Table S2 lists the primers for qPCR analysis in this study.

Acknowledgments

We thank Dr. Junying Yuan and Dr. Bisen Ding for providing suggestions and critically reading the manuscript. We would also like to thank Dr. Shuang Geng and Dr. Yanyi Huang for their kind help with SMART-seq library preparation. We extend our gratitude to Dr. Yang Geng for her tremendous support with imaging.

This work was supported by the National Science Foundation of China (No.92042304 to J. Wang and J. Hu; No.31872797 to J. Hu) and the Shanghai Municipal Science and Technology Major Project (No. 2019SHZDZX02).

Author contributions: J. Hu conceived the idea and supervised the study. J. Hu, H. He, M. Singhal, and H.G. Augustin designed the intercellular crosstalk analysis. H. He, W. Yang, N. Su, C. Zhang, and J. Dai performed the mouse experiments and analyzed the data. H. He performed the microfluidic chip assay and analyzed the images. H. He, Z. Li, and W. Wei performed bioinformatic analysis. F. Han prepared the sequencing libraries. H. He, J. Hu, W. Xia, and C. Liu performed electron microscope analysis. N. Su, M. Singhal, X. Zhu, and X. Liu performed the Western blot. J. Zhu measured the blood pressure. W. Bai and J. Wang performed intravital pulmonary imaging. H. He and N. Su. analyzed the alveolar capillary diameter. D. Chen and Z. Wang determined the Riociguat concentration in the lungs and plasma. W. Huang and F. Kirchhoff generated the *Cspg4-CreER^{T2}* mice and Z. Li generated the *Gucy1b1^{flox}* mice. J. Huan, H. He, W. Yang, and N. Su wrote the manuscript. All of the authors discussed the results and commented on the manuscripts.

Disclosures: The authors declare no competing interests exist.

Submitted: 2 July 2021
Revised: 20 September 2022
Accepted: 27 October 2022

References

Ahluwalia, A., P. Foster, R.S. Scotland, P.G. McLean, A. Mathur, M. Perretti, S. Moncada, and A.J. Hobbs. 2004. Antiinflammatory activity of soluble guanylate cyclase: cGMP-dependent down-regulation of P-selectin expression and leukocyte recruitment. *Proc. Natl. Acad. Sci. USA*. 101: 1386–1391. https://doi.org/10.1073/pnas.0304264101

Armulik, A., G. Genové, M. Mäe, M.H. Nisancioglu, E. Wallgard, C. Niaudet, L. He, J. Norlin, P. Lindblom, K. Strittmatter, et al. 2010. Pericytes regulate the blood-brain barrier. *Nature*. 468:557–561. https://doi.org/10.1038/nature09522

Augustin, H.G., G.Y. Koh, G. Thurston, and K. Alitalo. 2009. Control of vascular morphogenesis and homeostasis through the angiopoietin-Tie system. *Nat. Rev. Mol. Cell Biol.* 10:165–177. https://doi.org/10.1038/nrm2639

Becker, E.M., P. Schmidt, M. Schramm, H. Schroder, U. Walter, M. Hoenicka, R. Gerzer, and J.P. Stasch. 2000. The vasodilator-stimulated phosphoprotein (VASP): Target of YC-1 and nitric oxide effects in human and rat platelets. *J. Cardiovasc. Pharmacol.* 35:390–397. https://doi.org/10.1097/00005344-200003000-00007

Benz, P.M., C. Blume, S. Seifert, S. Wilhelm, J. Waschke, K. Schuh, F. Gertler, T. Munzel, and T. Renne. 2009. Differential VASP phosphorylation controls remodeling of the actin cytoskeleton. *J. Cell Sci.* 122:3954–3965. https://doi.org/10.1242/jcs.044537

Bettaga, N., R. Jager, S. Dunnes, D. Groneberg, and A. Friebe. 2015. Cell-specific impact of nitric oxide-dependent guanylyl cyclase on arteriogenesis and angiogenesis in mice. *Angiogenesis*. 18:245–254. https://doi.org/10.1007/s10456-015-9463-8

Cala-Garcia, J.D., J.D. Sierra-Breton, J.E. Cavelier-Baiz, A.A. Faccini-Martinez, and C.E. Perez-Diaz. 2020. Recovery of COVID-19 acute respiratory distress syndrome with tocilizumab: Successful outcome in two critically ill patients. *Immunotherapy*. 12:1127–1132. https://doi.org/10.2217/imt-2020-0154

Copin, M.C., E. Parmentier, T. Duburcq, J. Poissy, D. Mathieu, C.-I. Lille, and G. Anatomopathology. 2020. Time to consider histologic pattern of lung injury to treat critically ill patients with COVID-19 infection. *Intensive Care Med.* 46:1124–1126. https://doi.org/10.1007/s00134-020-06057-8

Daneman, R., L. Zhou, A.A. Kebede, and B.A. Barres. 2010. Pericytes are required for blood-brain barrier integrity during embryogenesis. *Nature.* 468:562–566. https://doi.org/10.1038/nature09513

Duan, L., X.D. Zhang, W.Y. Miao, Y.J. Sun, G. Xiong, Q. Wu, G. Li, P. Yang, H. Yu, H. Li, et al. 2018. PDGFRβ cells rapidly relay inflammatory signal from the circulatory system to neurons via chemokine CCL2. *Neuron.* 100:183–200.e8. https://doi.org/10.1016/j.neuron.2018.08.030

Ehrentraut, S., S. Frede, H. Stapel, T. Mengden, C. Grohe, J. Fandrey, R. Meyer, and G. Baumgarten. 2007. Antagonism of lipopolysaccharide-induced blood pressure attenuation and vascular contractility. *Arterioscler. Thromb. Vasc. Biol.* 27:2170–2176. https://doi.org/10.1161/ATVBAHA.107.146100

Evgenov, O.V., P. Pacher, P.M. Schmidt, G. Haskó, H.H.H.W. Schmidt, and J.-P. Stasch. 2006. NO-Independent stimulators and activators of soluble guanylate cyclase: Discovery and therapeutic potential. *Nat. Rev. Drug Discov.* 5:755–768. https://doi.org/10.1038/nrd2038

Figueiredo, A.M., P. Villacampa, R. Dieguez-Hurtado, J.J. Lozano, P. Kobialka, A.R. Cortazar, A. Martinez-Romero, A. Angulo-Urarte, C.A. Franco, M. Claret, et al. 2020. PI3Kbeta-regulated pericyte maturation governs vascular remodeling. *Circulation.* 142:688–704. https://doi.org/10.1161/CIRCULATIONAHA.119.042354

Flores-Costa, R., M. Duran-Guell, M. Casulleras, C. Lopez-Vicario, J. Alcaraz-Quiles, A. Diaz, J.J. Lozano, E. Titos, K. Hall, R. Sarno, et al. 2020. Stimulation of soluble guanylate cyclase exerts antiinflammatory actions in the liver through a VASP/NF-κB/NLRP3 inflammasome circuit. *Proc. Natl. Acad. Sci. USA.* 117:28263–28274. https://doi.org/10.1073/pnas.2000466117

Fukutani, T., S. Iino, and Y. Nojyo. 2009. The expression of soluble guanylate cyclase in the vasculature of rat skeletal muscle. *Arch. Histol. Cytol.* 72:117–126. https://doi.org/10.1679/aohc.72.117

Gau, D., and P. Roy. 2018. SRF'ing and SAP'ing: The role of MRTF proteins in cell migration. *J. Cell Sci.* 131:jcs218222. https://doi.org/10.1242/jcs.218222

Guo, Y., B.D. Jardin, P. Zhou, I. Sethi, B.N. Akerberg, C.N. Toepfer, Y. Ai, Y. Li, Q. Ma, S. Guatimosim, et al. 2018. Hierarchical and stage-specific regulation of murine cardiomyocyte maturation by serum response factor. *Nat. Commun.* 9:3837. https://doi.org/10.1038/s41467-018-06347-2

Hall, K.C., S.G. Bernier, S. Jacobson, G. Liu, P.Y. Zhang, R. Sarno, V. Catanzano, M.G. Currie, and J.L. Masferrer. 2019. sGC stimulator praliciguat suppresses stellate cell fibrotic transformation and inhibits fibrosis and inflammation in models of NASH. *Proc. Natl. Acad. Sci. USA.* 116:11057–11062. https://doi.org/10.1073/pnas.1821045116

Hammes, H.P., J. Lin, P. Wagner, Y. Feng, F. Vom Hagen, T. Krzizok, O. Renner, G. Breier, M. Brownlee, and U. Deutsch. 2004. Angiopoietin-2 causes pericyte dropout in the normal retina: Evidence for involvement in diabetic retinopathy. *Diabetes.* 53:1104–1110. https://doi.org/10.2337/diabetes.53.4.1104

Han, S., S.-J. Lee, K.E. Kim, H.S. Lee, N. Oh, I. Park, E. Ko, S.J. Oh, Y.-S. Lee, D. Kim, et al. 2016. Amelioration of sepsis by TIE2 activation-induced vascular protection. *Sci. Transl. Med.* 8:335ra55. https://doi.org/10.1126/scitranslmed.aad9260

Harbeck, B., S. Huttelmaier, K. Schluter, B.M. Jockusch, and S. Illenberger. 2000. Phosphorylation of the vasodilator-stimulated phosphoprotein regulates its interaction with actin. *J. Biol. Chem.* 275:30817–30825. https://doi.org/10.1074/jbc.M005066200

He, L., M. Vanlandewijck, E. Raschperger, M. Andaloussi Mae, B. Jung, T. Lebouvier, K. Ando, J. Hofmann, A. Keller, and C. Betsholtz. 2016. Analysis of the brain mural cell transcriptome. *Sci. Rep.* 6:35108. https://doi.org/10.1038/srep35108

Huang, W., N. Zhao, X. Bai, K. Karram, J. Trotter, S. Goebbels, A. Scheller, and F. Kirchhoff. 2014. Novel NG2-CreERT2 knock-in mice demonstrate heterogeneous differentiation potential of NG2 glia during development. *Glia.* 62:896–913. https://doi.org/10.1002/glia.22648

Hurtado-Alvarado, G., A.M. Cabanas-Morales, and B. Gomez-Gonzalez. 2014. Pericytes: Brain-immune interface modulators. *Front. Integr. Neurosci.* 7:80. https://doi.org/10.3389/fnint.2013.00080

Joutel, A., C. Corpechot, A. Ducros, K. Vahedi, H. Chabriat, P. Mouton, S. Alamowitch, V. Domenga, M. Cecillion, E. Marechal, et al. 1996. Notch3 mutations in CADASIL, a hereditary adult-onset condition causing stroke and dementia. *Nature.* 383:707–710. https://doi.org/10.1038/383707a0

Kay, E., L. Gomez-Garcia, A. Woodfin, R.S. Scotland, and J.R. Whiteford. 2015. Sexual dimorphisms in leukocyte trafficking in a mouse peritonitis model. *J. Leukoc. Biol.* 98:805–817. https://doi.org/10.1189/jlb.3A1214-601RR

Kim, S., H. Lee, M. Chung, and N.L. Jeon. 2013. Engineering of functional, perfusable 3D microvascular networks on a chip. *Lab Chip.* 13:1489–1500. https://doi.org/10.1039/c3lc41320a

Leveen, P., M. Pekny, S. Gebre-Medhin, B. Swolin, E. Larsson, and C. Betsholtz. 1994. Mice deficient for PDGF B show renal, cardiovascular, and hematological abnormalities. *Genes Dev.* 8:1875–1887. https://doi.org/10.1101/gad.8.16.1875

Machuca-Parra, A.I., A.A. Bigger-Allen, A.V. Sanchez, A. Boutabla, J. Cardona-Velez, D. Amarnani, M. Saint-Geniez, C.W. Siebel, L.A. Kim, P.A. D'Amore, and J.F. Arboleda-Velasquez. 2017. Therapeutic antibody targeting of Notch3 signaling prevents mural cell loss in CADASIL. *J. Exp. Med.* 214:2271–2282. https://doi.org/10.1084/jem.20161715

Matthay, M.A., R.L. Zemans, G.A. Zimmerman, Y.M. Arabi, J.R. Beitler, A. Mercat, M. Herridge, A.G. Randolph, and C.S. Calfee. 2019. Acute respiratory distress syndrome. *Nat. Rev. Dis. Primers*:1–22. https://doi.org/10.1038/s41572-019-0069-0

Morikawa, S., P. Baluk, T. Kaidoh, A. Haskell, R.K. Jain, and D.M. McDonald. 2002. Abnormalities in pericytes on blood vessels and endothelial sprouts in tumors. *Am. J. Pathol.* 160:985–1000. https://doi.org/10.1016/S0002-9440(10)64920-6

Park-Windhol, C., and P.A. D'Amore. 2016. Disorders of vascular permeability. *Annu. Rev. Pathol.* 11:251–281. https://doi.org/10.1146/annurev-pathol-012615-044506

Picelli, S., O.R. Faridani, A.K. Bjorklund, G. Winberg, S. Sagasser, and R. Sandberg. 2014. Full-length RNA-seq from single cells using Smart-seq2. *Nat. Protoc.* 9:171–181. https://doi.org/10.1038/nprot.2014.006

Ramilowski, J.A., T. Goldberg, J. Harshbarger, E. Kloppmann, M. Lizio, V.P. Satagopam, M. Itoh, H. Kawaji, P. Carninci, B. Rost, et al. 2016. Corrigendum: A draft network of ligand-receptor-mediated multicellular signalling in human. *Nat. Commun.* 7:10706. https://doi.org/10.1038/ncomms10706

Rustenhoven, J., D. Jansson, L.C. Smyth, and M. Dragunow. 2017. Brain pericytes as mediators of neuroinflammation. *Trends Pharmacol. Sci.* 38:291–304. https://doi.org/10.1016/j.tips.2016.12.001

Schwappacher, R., A. Kilic, B. Kojonazarov, M. Lang, T. Diep, S. Zhuang, T. Gawlowski, R.T. Schermuly, A. Pfeifer, G.R. Boss, and R.B. Pilz. 2013. A molecular mechanism for therapeutic effects of cGMP-elevating agents in pulmonary arterial hypertension. *J. Biol. Chem.* 288:16557–16566. https://doi.org/10.1074/jbc.M113.458729

Sheikh, B.N., S. Guhathakurta, T.H. Tsang, M. Schwabenland, G. Renschler, B. Herquel, V. Bhardwaj, H. Holz, T. Stehle, O. Bondareva, et al. 2020. Neural metabolic imbalance induced by MOF dysfunction triggers pericyte activation and breakdown of vasculature. *Nat. Cell Biol.* 22:828–841. https://doi.org/10.1038/s41556-020-0526-8

Shen, J., M. Frye, B.L. Lee, J.L. Reinardy, J.M. McClung, K. Ding, M. Kojima, H. Xia, C. Seidel, R. Lima e Silva, et al. 2014. Targeting VE-PTP activates TIE2 and stabilizes the ocular vasculature. *J. Clin. Invest.* 124:4564–4576. https://doi.org/10.1172/JCI74527

Stasch, J.P., P. Pacher, and O.V. Evgenov. 2011. Soluble guanylate cyclase as an emerging therapeutic target in cardiopulmonary disease. *Circulation.* 123:2263–2273. https://doi.org/10.1161/CIRCULATIONAHA.110.981738

Suri, C., P.F. Jones, S. Patan, S. Bartunkova, P.C. Maisonpierre, S. Davis, T.N. Sato, and G.D. Yancopoulos. 1996. Requisite role of angiopoietin-1, a ligand for the TIE2 receptor, during embryonic angiogenesis. *Cell.* 87:1171–1180. https://doi.org/10.1016/s0092-8674(00)81813-9

Teuwen, L.A., V. Geldhof, A. Pasut, and P. Carmeliet. 2020. COVID-19: The vasculature unleashed. *Nat. Rev. Immunol.* 20:389–391. https://doi.org/10.1038/s41577-020-0343-0

Theilig, F., M. Bostanjoglo, H. Pavenstadt, C. Grupp, G. Holland, I. Slosarek, A.M. Gressner, M. Russwurm, D. Koesling, and S. Bachmann. 2001. Cellular distribution and function of soluble guanylyl cyclase in rat kidney and liver. *J. Am. Soc. Nephrol.* 12:2209–2220. https://doi.org/10.1681/ASN.V12112209

Thompson, B.T., R.C. Chambers, and K.D. Liu. 2017. Acute respiratory distress syndrome. *N. Engl. J. Med.* 377:1904–1905. https://doi.org/10.1056/NEJMc1711824

Thurston, G., C. Suri, K. Smith, J. McClain, T.N. Sato, G.D. Yancopoulos, and D.M. McDonald. 1999. Leakage-resistant blood vessels in mice transgenically overexpressing angiopoietin-1. *Science.* 286:2511–2514. https://doi.org/10.1126/science.286.5449.2511

Tilley, A.E., M.S. Walters, R. Shaykhiev, and R.G. Crystal. 2015. Cilia dysfunction in lung disease. *Annu. Rev. Physiol.* 77:379–406. https://doi.org/10.1146/annurev-physiol-021014-071931

Torok, O., B. Schreiner, J. Schaffenrath, H.C. Tsai, U. Maheshwari, S.A. Stifter, C. Welsh, A. Amorim, S. Sridhar, S.G. Utz, et al. 2021. Pericytes regulate vascular immune homeostasis in the CNS. *Proc. Natl. Acad. Sci. USA.* 118:e2016587118. https://doi.org/10.1073/pnas.2016587118

Uemura, A., M. Ogawa, M. Hirashima, T. Fujiwara, S. Koyama, H. Takagi, Y. Honda, S.J. Wiegand, G.D. Yancopoulos, and S.I. Nishikawa. 2002. Recombinant angiopoietin-1 restores higher-order architecture of growing blood vessels in mice in the absence of mural cells. *J. Clin. Invest.* 110: 1619–1628. https://doi.org/10.1172/JCI15621

Vanlandewijck, M., L. He, M.A. Mäe, J. Andrae, K. Ando, F. Del Gaudio, K. Nahar, T. Lebouvier, B. Laviña, L. Gouveia, et al. 2018. A molecular atlas of cell types and zonation in the brain vasculature. *Nature*. 554:475–480. https://doi.org/10.1038/nature25739

Villar, J., C. Ferrando, D. Martinez, A. Ambros, T. Munoz, J.A. Soler, G. Aguilar, F. Alba, E. Gonzalez-Higueras, L.A. Conesa, et al. 2020. Dexamethasone treatment for the acute respiratory distress syndrome: A multicentre, randomised controlled trial. *Lancet Respir. Med.* 8:267–276. https://doi.org/10.1016/S2213-2600(19)30417-5

Wang, Y., L. Pan, C.B. Moens, and B. Appel. 2014. Notch3 establishes brain vascular integrity by regulating pericyte number. *Development*. 141: 307–317. https://doi.org/10.1242/dev.096107

Weinberg, J.R., P. Boyle, A. Meager, and A. Guz. 1992. Lipopolysaccharide, tumor necrosis factor, and interleukin-1 interact to cause hypotension. *J. Lab. Clin. Med.* 120:205–211

Xiang, B., G. Zhang, L. Guo, X.A. Li, A.J. Morris, A. Daugherty, S.W. Whiteheart, S.S. Smyth, and Z. Li. 2013. Platelets protect from septic shock by inhibiting macrophage-dependent inflammation via the cyclooxygenase 1 signalling pathway. *Nat. Commun.* 4:2657. https://doi.org/10.1038/ncomms3657

Xu, Z., L. Shi, Y. Wang, J. Zhang, L. Huang, C. Zhang, S. Liu, P. Zhao, H. Liu, L. Zhu, et al. 2020. Pathological findings of COVID-19 associated with acute respiratory distress syndrome. *Lancet Respir. Med.* 8:420–422. https://doi.org/10.1016/S2213-2600(20)30076-X

Yang, W., H. He, T. Wang, N. Su, F. Zhang, K. Jiang, J. Zhu, C. Zhang, K. Niu, L. Wang, et al. 2021. Single-cell transcriptomic analysis reveals a hepatic stellate cell-activation roadmap and myofibroblast origin during liver fibrosis in mice. *Hepatology*. 74:2774–2790. https://doi.org/10.1002/hep.31987

Zhang, G., B. Xiang, A. Dong, R.C. Skoda, A. Daugherty, S.S. Smyth, X. Du, and Z. Li. 2011. Biphasic roles for soluble guanylyl cyclase (sGC) in platelet activation. *Blood*. 118:3670–3679. https://doi.org/10.1182/blood-2011-03-341107

Zimmer, D.P., C.M. Shea, J.V. Tobin, B. Tchernychev, P. Germano, K. Sykes, A.R. Banijamali, S. Jacobson, S.G. Bernier, R. Sarno, et al. 2020. Olinciguat, an oral sGC stimulator, exhibits diverse pharmacology across preclinical models of cardiovascular, metabolic, renal, and inflammatory disease. *Front. Pharmacol.* 11:419. https://doi.org/10.3389/fphar.2020.00419

Supplemental material

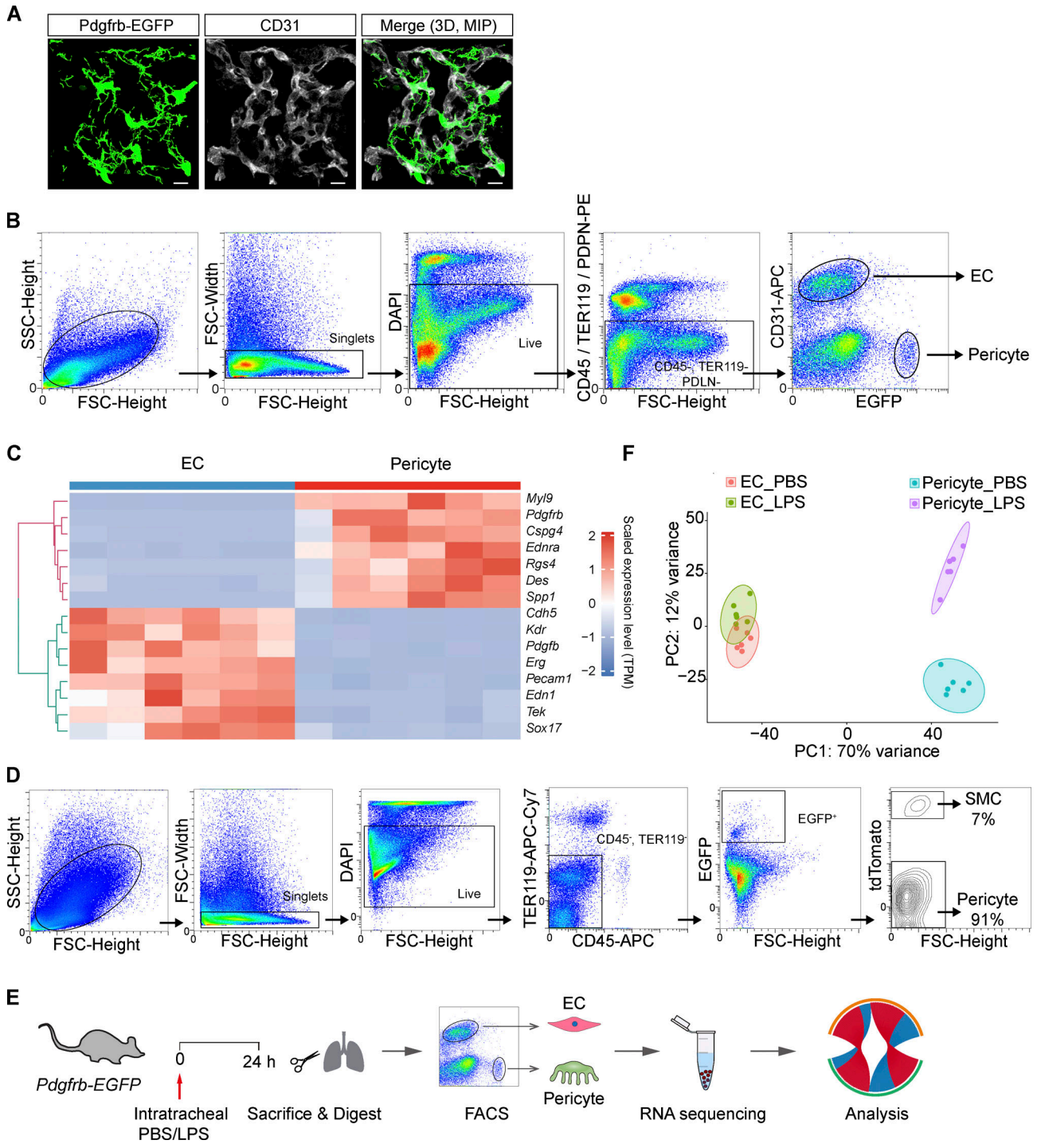

Figure S1. **Isolation and RNA-seq analysis of ECs and pericytes from the lungs of healthy and LPS-instilled *Pdgfrb-EGFP* mice. (A)** Fluorescent images showing the morphology of EGFP-positive pericytes in the lungs of a *Pdgfrb-EGFP* mouse. Lung sections were co-stained with EC-specific marker CD31. Scale bar: 10 µm. **(B)** FACS gating strategy for the isolation of ECs and pericytes from *Pdgfrb-EGFP* mice. **(C)** Heatmap illustrating the row-normalized expression of EC- and pericyte-specific markers (n = 6 mice per group). **(D)** FACS quantification of the percentage of pericytes ($EGFP^+$) and vSMCs ($EGFP^+tdTomato^+$) in the lungs of *Pdgfrb-EGFP::SM22a-CreER^{T2}::Rosa26-tdTomato* mice. **(E)** Schematic illustration depicting the workflow for EC and pericyte isolation, RNA-seq, and interactome analysis. **(F)** PCA of the DEGs in ECs and pericytes isolated from the lungs of control or LPS-instilled *Pdgfrb-EGFP* mice (n = 6 mice per group).

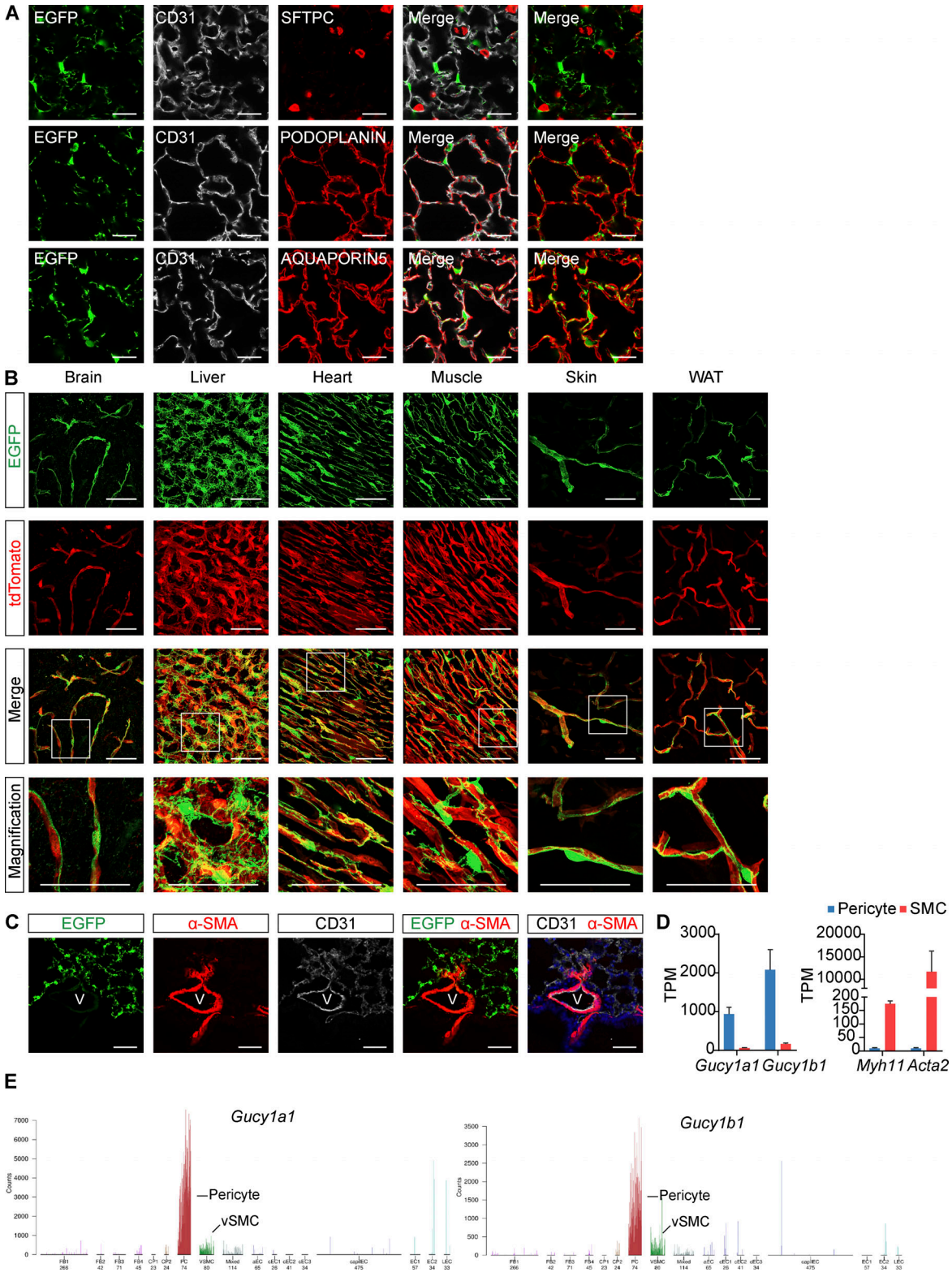

Figure S2. **Gucy1a1-EGFP is highly expressed in the pericytes of multiple organs. (A)** Representative immunofluorescent images of lung sections of Gucy1a1-EGFP mice co-stained with EC-specific marker CD31 and type-I (PODOPLANIN + or AQUAPORIN5+) or type-II alveolar epithelial cells (SFTPC+). Scale bar: 25 µm. **(B)** Representative fluorescent images showing the EGFP and tdTomato expression pattern in brain, liver, heart, muscle, skin, and white adipose tissue (WAT) of *Gucy1a1-EGFP::Tek-Cre::Rosa26-tdTomato mice*, with EGFP-labeled pericytes and tdTomato-labeled ECs. Scale bar: 50 µm. **(C)** Representative images of lung sections of *Gucy1a1-EGFP* mice stained with EC-specific CD31 and SMC-specific α-SMA antibodies. EGFP was expressed at very low levels in vSMCs in the lung. Scale bar: 50 µm. **(D)** Plots depicting TPM values of *Gucy1a1*, *Gucy1b1*, *Myh11*, and *Acta2* in pericytes and vSMCs isolated from *Gucy1a1-EGFP::SM22a- CreER^{T2}::ROSA26-tdTomato* mice. Data are presented as mean ± SD, *n* = 3 mice. **(E)** Lung single-cell RNA-seq data showing the *Gucy1a1* and *Gucy1b1* expression levels in various lung cell types (Vanlandewijck et al., 2018).

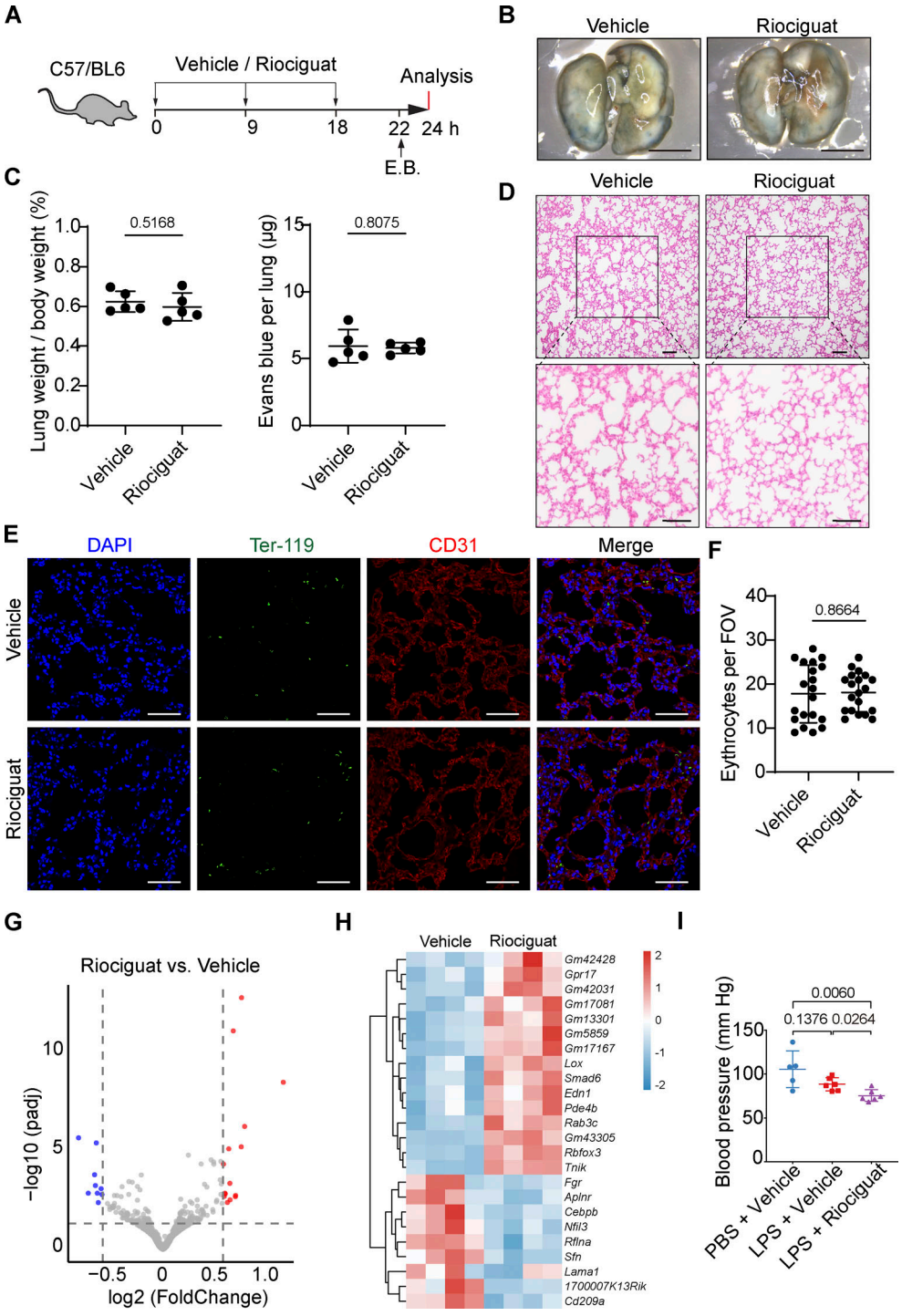

Figure S3. **Riociguat does not affect lung function in healthy mice. (A)** Schematic illustration depicting the Riociguat treatment regimen in WT mice. E.B.: Evans blue. **(B)** Macro images of lungs isolated from PBS- or Riociguat-treated mice that received Evans blue dye infusion before sacrifice. Scale bar: 5 mm. **(C)** Quantification of lung weight/body weight ratio and the remaining amount of Evans blue in the lungs of PBS- or Riociguat-treated WT mice. Data are shown as the mean ± SD, *n* = 5 mice per group. **(D)** Representative images showing the H&E stained lung sections of PBS- or Riociguat-treated mice. Scale bar: 100 μm. **(E)** Representative immunofluorescence images showing the lung sections of PBS- or Riociguat-treated mice that were stained with DAPI (nuclei), Ter119 (erythrocyte), and CD31 (EC). Scale bar: 50 μm. **(F)** Quantification showing Ter119 stained erythrocyte number in the lung sections. **(G)** Volcano plot showing the DEGs in the Riociguat-treated lungs compared to controls. **(H)** Heatmap showing the individual DEGs in the Riociguat-treated lungs vs control lungs. **(I)** Dot plot showing the blood pressure of mice received PBS + vehicle, LPS + vehicle, or LPS + Riociguat treatment. Data are shown as the mean ± SD, *n* = 5–6 mice per group. Statistical significance was determined by two-tailed Student's *t* test (C and F) or one-way ANOVA with Tukey test (I). P < 0.05 was considered statistically significant.

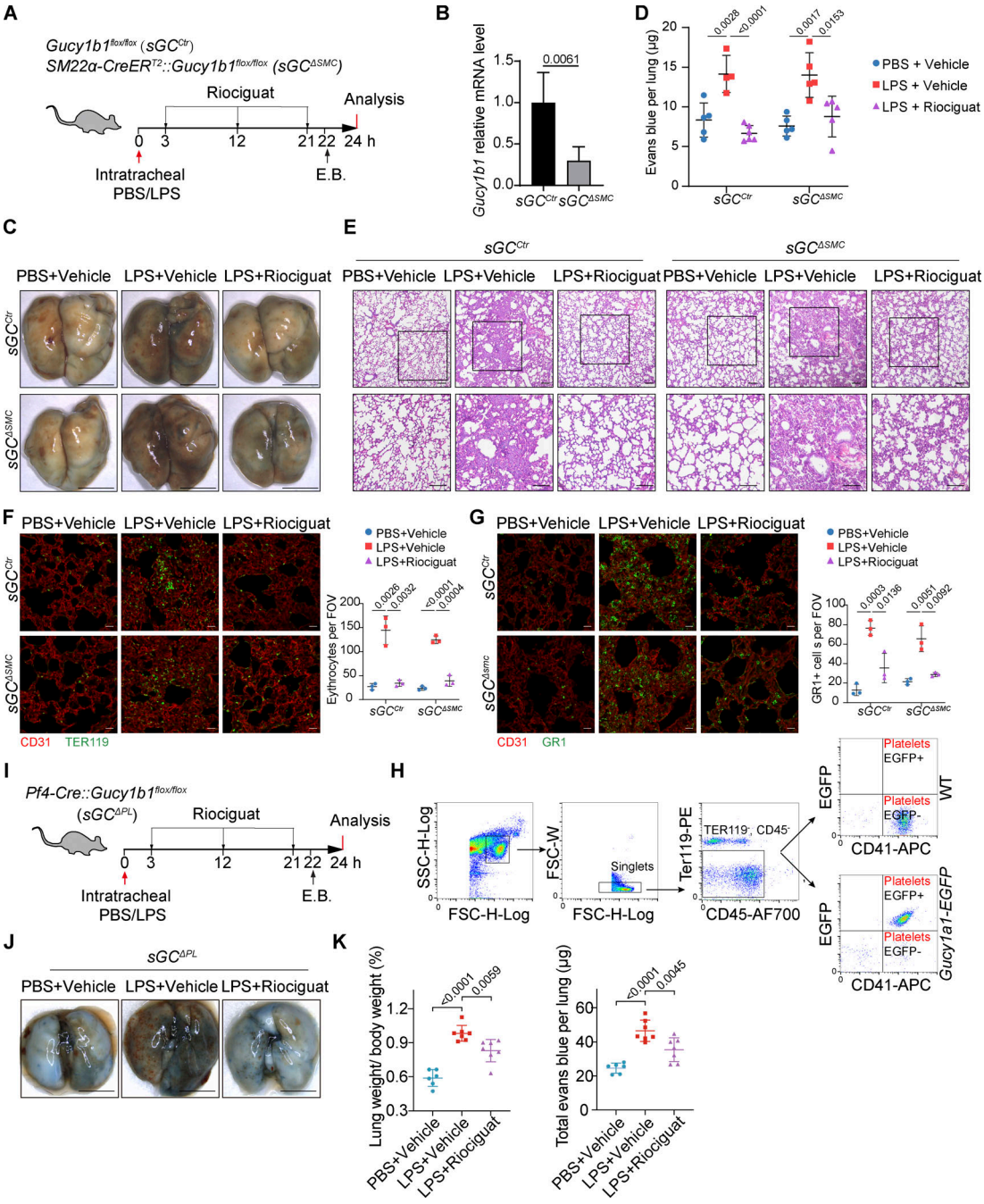

Figure S4. **vSMC- or platelet-specific sGC inactivation does not abolish Riociguat's lung protection effects. (A)** Schematic illustration depicting the Riociguat treatment in the *Gucy1b1*$^{flox/fox}$ (*sGC*^{Ctr}) and *SM22α-CreER*^{T2}*::Gucy1b1*$^{flox/fox}$ (*sGC*^{ΔSMC}) mice received intratracheal PBS/LPS instillation. E.B.: Evans blue. **(B)** qPCR analysis of *Gucy1b1* relative expression levels in the arteries of *sGC*^{Ctr} and *sGC*^{ΔSMC} mice. Data are shown as the mean ± SD, *n* = 4–5 mice. **(C)** Macro images of the lungs of Evans blue–perfused *sGC*^{Ctr} and *sGC*^{ΔSMC} mice treated with PBS + vehicle, LPS + vehicle, or LPS + Riociguat. Scale bar: 5 mm. **(D)** Quantification of the remaining amount of Evans blue in the lungs of PBS + vehicle–, LPS + vehicle–, or LPS + Riociguat–treated *sGC*^{Ctr} and *sGC*^{ΔSMC} mice. Data are shown as the mean ± SD, *n* = 4–6 mice per group. **(E)** Representative images showing the H&E stained lung sections of PBS + vehicle–, LPS + vehicle–, or LPS + Riociguat–treated *sGC*^{Ctr} *and sGC*^{ΔSMC} mice. Scale bar: 100 μm. **(F)** Representative fluorescence images showing CD31 and TER119 stained lung sections of *sGC*^{Ctr} *and sGC*^{ΔSMC} mice treated with PBS + vehicle, LPS + vehicle, or LPS + Riociguat and quantification of TER119-positive erythrocytes in the lung section per FOV. Scale bar: 20 μm. Data are shown as the mean ± SD, *n* = 3 mice. **(G)** Representative fluorescence images showing CD31 and GR1 stained lung sections of *sGC*^{Ctr} *and sGC*^{ΔSMC} mice treated with PBS + vehicle, LPS + vehicle, or LPS + Riociguat and quantification of GR1-positive neutrophils in the lung section per FOV. Scale bar: 20 μm. Data are shown as the mean ± SD, *n* = 3 mice. **(H)** FACS analysis of the blood of Gucy1a1-EGFP mice reveals that EGFP was expressed in platelets. The blood of WT mice served as negative control. **(I)** Schematic illustration depicting the Riociguat treatment in the PBS/LPS instilled *Pf4-Cre::Gucy1b1*$^{flox/flox}$ (*sGC*^{ΔPL}, platelet-specific sGC inactivation) mice. **(J)** Macro images of the lungs of Evans blue–perfused *sGC*^{ΔPL} mice treated with PBS + vehicle, LPS + vehicle, or LPS + Riociguat. Scale bar: 5 mm. **(K)** Quantification of leaked Evans blue in the lungs and the lung weight/body weight ratio of *sGC*^{ΔPL} mice treated with PBS + vehicle, LPS + vehicle, or LPS + Riociguat. Data are shown as the mean ± SD, *n* = 6–7 mice. Statistical significance was determined by two-tailed Student's *t* test (B) or one-way ANOVA with Tukey test (D, F, G, and K). P < 0.05 was considered statistically significant.

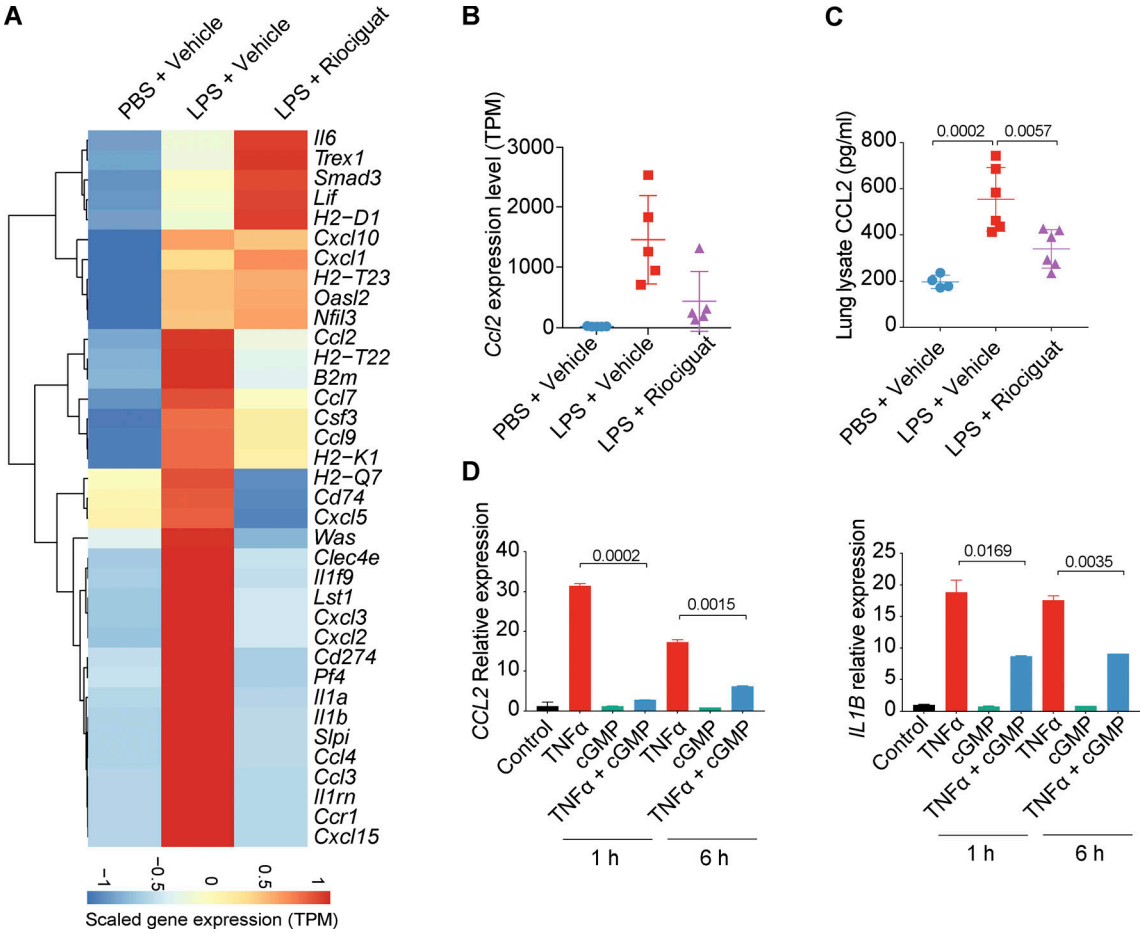

Figure S5. **Riociguat suppresses LPS-induced inflammatory cytokine expression in pericytes. (A)** Heatmap depicting the differentially expressed inflammatory cytokines in lung pericytes isolated from PBS + vehicle–, LPS + vehicle–, and LPS + Riociguat–treated mice. Data are presented as the mean of each gene expression values of five mice. **(B)** Plot showing the *Ccl2* expression levels (TPM) in lung pericytes isolated from PBS + vehicle–, LPS + vehicle–, and LPS + Riociguat–treated mice. **(C)** The protein levels of CCL2 in lung lysates of mice received PBS + vehicle, LPS + vehicle, and LPS + Riociguat treatments were measured using ELISA. Data are shown as the mean ± SD, *n* = 4–6 mice per group. **(D)** HBVPs were stimulated with TNFα, cGMP, or TNFα + cGMP. The expression levels of *CCL2* and *IL1B* 1 or 6 h after stimulation were determined using qPCR. Data are shown as the mean ± SD. Statistical significance was determined by one-way ANOVA with Tukey test (B–D). $P < 0.05$ was considered statistically significant.

Provided online are two tables. Table S1 lists the primers for genotyping. Table S2 lists the primers for qPCR analysis in this study.